Journal of Materials Chemistry A

REVIEW

View Article Online
View Journal | View Issue

Cite this: J. Mater. Chem. A, 2022, 10, 19254

Development of catalysts and electrolyzers toward industrial-scale CO_2 electroreduction

Geng Li,[a] Yong Liu,[a] Qiang Zhang,[a] Qiushi Hu,[a] Weihua Guo,[a] Xiaohu Cao,[a] Yubing Dou,[a] Le Cheng,[a] Yun Song,[a] Jianjun Su,[a] Libei Huang[a] and Ruquan Ye *[ab]

The electrochemical CO_2 reduction reaction (CO_2RR) has attracted significant research interest in recent years due to its potential to mitigate carbon emissions while providing valuable fuels and chemicals. The performance of the CO_2RR has been improved from tens of milliamperes per square centimeter to orders of magnitude higher, with selectivity approaching 100% for some products. This review will highlight the key development of the CO_2RR toward industrially relevant performance. We will first discuss the recent advances of electrocatalysts in refining the product's selectivity. A few representative electrocatalysts will be showcased, including metal-free catalysts, metal nanoparticles, and molecular catalysts and their derivatives. Then we will show the development of electrochemical cells for the CO_2RR, which play a pivotal role in achieving a current density of amperes per square centimeter. Specifically, using the flow electrolyzer has significantly improved the CO_2RR current densities compared to the conventional H-type cell. Lastly, we will provide perspectives on future development and challenges of the CO_2RR.

Received 16th March 2022
Accepted 27th May 2022

DOI: 10.1039/d2ta02086f

rsc.li/materials-a

1. Introduction

The balance of the global carbon cycle has been disrupted by the overconsumption of fuels and increasing emissions of CO_2, eventually resulting in a slew of ecological and environmental issues, such as global warming and the rise of sea levels.[1,2] Limiting CO_2 generation and turning it into valuable chemicals appear to be essential to mitigate the crisis. So far, several techniques have been developed to address the carbon emission problem, including CO_2 capture,[3,4] storage,[5–7] and conversion.[8–11] The electrochemical CO_2 reduction reaction (CO_2RR), coupled with renewable energy sources such as wind and solar energy, has been recognized as one of the optimum approaches to achieve carbon neutrality (Fig. 1).[12,13] The utilization of photovoltaic and wind power in electrochemical CO_2RR systems

[a]Department of Chemistry, State Key Laboratory of Marine Pollution, City University of Hong Kong, Hong Kong 999077, China. E-mail: ruquanye@cityu.edu.hk
[b]City University of Hong Kong Shenzhen Research Institute, Shenzhen, Guangdong 518057, China

Geng Li is currently a graduate student in Chemistry, City University of Hong Kong. He obtained his bachelor's and master's degrees from Nanjing University of Science and Technology in 2018 and University of Science and Technology of China in 2021, respectively. His current research interest is focused on the carbon dioxide electroreduction reaction mechanism and device design.

Ruquan Ye is an assistant professor in Chemistry, City University of Hong Kong. He received his B.S. (Chemistry) in 2012 from Hong Kong University of Science and Technology under Prof. Ben Zhong Tang's supervision, and his PhD (Chemistry) in 2017 from Rice University mentored by Prof. James M. Tour. He worked with Prof. Karthish Manthiram as a postdoctoral associate in Chemical Engineering at the Massachusetts Institute of Technology (2017–2018). His research interests include developing cost-effective methods for materials manufacturing and investigating their applications in energy and environmental science.

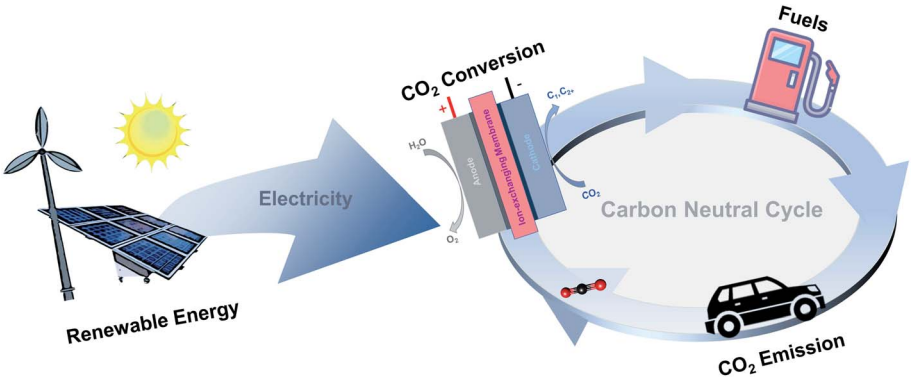

Fig. 1 A schematic diagram of the electrochemical CO_2RR to chemical fuels from renewable energy sources.

can simultaneously reduce the atmospheric CO_2 concentration and convert the intermittent and unstable electricity into chemical fuels. Furthermore, as the cost of power generated by photovoltaic systems and wind turbines continues to drop, the electrochemical CO_2RR is emerging as an attractive and sustainable technique for converting atmospheric CO_2 into fuels and chemicals.

The electrocatalytic CO_2RR is a complicated process that involves multiproton-coupled electron transfer and produces mixtures of reduction products. Based on the number of carbon atoms, CO_2RR products are classified into C_1 products including formate/formic acid (HCOOH), carbon monoxide (CO), methanol (CH_3OH) and methane (CH_4), C_2 products including ethylene (C_2H_4), ethanol (C_2H_5OH) and acetate (CH_3COOH), C_3 products such as propylene (C_3H_6) and *n*-propanal (C_2H_5CHO), and long-chain products. However, there exists an intractable problem that CO_2 is thermodynamically stable, leading to a large energy barrier for electrochemical CO_2 activation.[14] The electrochemical CO_2RR is generally started by transferring a single electron to a linear CO_2 molecule to generate bent $CO_2^{\bullet-}$, which requires a potential of -1.9 V *vs.* the standard hydrogen electrode (SHE) (eqn (1)), indicating high activation energy for the CO_2RR.[15] Despite the close potential for different products (eqn (2)–(7)), the electrochemical CO_2RR to hydrocarbons or oxygenates generally possesses a higher kinetic barrier than that of CO and HCOOH, since more electrons are required to form hydrocarbons or oxygenates.[16] Furthermore, the hydrogen evolution reaction (eqn (8)) will compete with the CO_2RR at the cathode, making it challenging to generate target products. Thus, designing and manufacturing CO_2RR electrocatalysts with high activity and faradaic efficiency (FE) for a particular product are critical for industrial applications. Novel high-efficiency catalysts including metal-free catalysts, metal nanoparticles, and molecular catalysts and their derivatives have been developed for the electrochemical CO_2RR in the last few decades.

$$CO_2 + e^- \rightarrow CO_2^{\bullet-},\ E_0 = -1.90\ \text{V} \quad (1)$$

$$CO_2 + 2H^+ + 2e^- \rightarrow CO + H_2O,\ E_0 = -0.53\ \text{V} \quad (2)$$

$$CO_2 + 2H^+ + 2e^- \rightarrow HCOOH,\ E_0 = -0.61\ \text{V} \quad (3)$$

$$CO_2 + 6H^+ + 6e^- \rightarrow CH_3OH + H_2O,\ E_0 = -0.38\ \text{V} \quad (4)$$

$$CO_2 + 8H^+ + 8e^- \rightarrow CH_4 + 2H_2O,\ E_0 = -0.24\ \text{V} \quad (5)$$

$$2CO_2 + 12H^+ + 12e^- \rightarrow C_2H_4 + 4H_2O,\ E_0 = -0.34\ \text{V} \quad (6)$$

$$2CO_2 + 12H^+ + 12e^- \rightarrow C_2H_5OH + 3H_2O,\ E_0 = -0.33\ \text{V} \quad (7)$$

$$2H^+ + 2e^- \rightarrow H_2,\ E_0 = -0.42\ \text{V} \quad (8)$$

Besides, the CO_2RR is mostly investigated using the typical H-type electrolytic cell in the laboratory. The current densities for the CO_2RR in this system are usually less than 50 mA cm^{-2} due to the low CO_2 solubility in aqueous solution (~0.03 mg kg^{-1} at ~300 K, 1 atm in water), whereas the industrial-scale current densities should be at least 200 mA cm^{-2}.[17,18] Recently, efforts in building direct gas-feed reactors have provided the possibility for electrocatalytic CO_2 conversion at industrial-scale current densities, presenting new insight on the technology's commercialization.[19] In this review, we first summarize the literature on representative electrocatalysts in refining the selectivity of different products, and then discuss the latest progress in electrolytic cells for industrial-scale CO_2RR. We also outline the challenges and prospects of this burgeoning research field.

2. CO_2RR catalysts for different products

The electroreduction process begins with the adsorption and activation of CO_2 on the surface of the catalyst, leading to the formation of *OHCO or *COOH intermediates (the atom with * binds to the surface) (Fig. 2). Then the *OHCO is further reduced to generate formic acid, while *COOH is reduced to *CO adsorbed on the catalyst surface. *CO will be easily desorbed as a gas product on the surface of catalysts with weak binding energies for *CO. Meanwhile, *CO can be further reduced to generate multi-electron products if it binds to the catalyst surface strongly. Considering the diversity of products, it is challenging to develop catalysts with high activity and

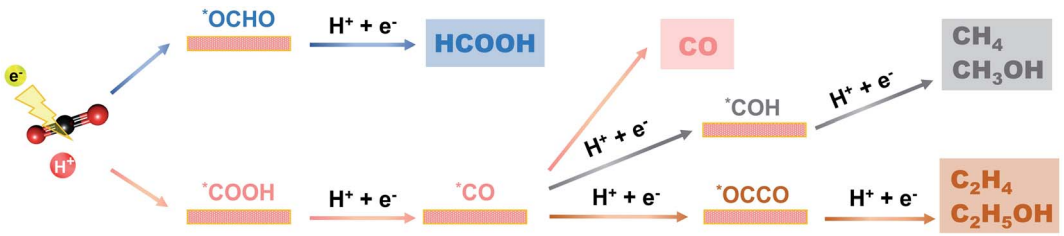

Fig. 2 Different pathways for the electrochemical CO_2RR.

selectivity. There are two main paths for further reduction of CO. The first one includes a succession of proton-coupled electron transfers that result in CH_3OH and CH_4 production. The second route begins with the dimerization of *CO to form *CO dimers followed by the hydrogenation process to generate C_{2+} products such as C_2H_4 and C_2H_5OH.[20,21]

So far, metal catalysts have been the most effective catalysts for the CO_2RR. Noble metals such as Au, Ag, and Pd, and non-noble metals like Zn show high catalytic activity towards CO_2-to-CO electroreduction, because of their weak binding energies for *CO.[22] p-Block metals, such as Sn, In, Bi, and Pd, and their composites, present a high selectivity for $HCOO^-$/HCOOH because of their favorable binding to *OHCO.[23] Cu is usually used for multi-electron transfer products (such as CH_4 and CH_3OH) and C_{2+} products because of its moderate binding energy of *CO, which is a crucial intermediate product involved in the C–C dimerization step.[24] However, bulk metals usually show low catalytic performance. In order to enhance the catalytic activity of metals, nanostructured metals with well-controlled morphologies and structures have been prepared for enhanced catalytic performances. In addition, metal alloying, which changes the adsorption to the intermediate, is another strategy to prepare highly active catalysts. More recently, single-atom catalysts (SACs) have also attracted increasing attention for the electrochemical CO_2RR, because of their maximized atomic usage and tunable activities.[25] Moreover, molecular catalysts and metal-free catalysts have also been developed to hinder the use of metals and decrease the preparation cost of catalysts. In this section, we will review representative electrocatalysts in refining the selectivity of different products.

2.1 Carbon monoxide

Among all the CO_2RR products, CO has been considered the most commercially viable product because of its kinetically accessible process (two-proton and two-electron reaction) and high efficiency. Moreover, CO is an essential and indispensable precursor for producing various commodity chemicals in industry. For example, synthesis gas with a 2 : 1 CO/H_2 ratio can be utilized to produce a variety of organic chemicals (such as higher hydrocarbons) *via* the Fischer–Tropsch process.[24,26]

So far, noble metals such as Au, Ag, and Pd, and non-noble metals like Zn have shown high catalytic activity towards CO_2-to-CO electroreduction. Ag is the representative metal catalyst that has been most extensively explored for CO generation due to its high activity. Generally, Ag nanoparticles show higher catalytic performance than bulk Ag.[27] Hwang *et al.*[28] reported a series of differently sized Ag nanoparticles anchored on a carbon support *via* a one-pot synthesis method. The results showed that 5 nm Ag nanoparticles presented 4-fold improved FE_{CO} compared to the Ag foil at −0.75 V *vs.* the reversible hydrogen electrode (RHE). Density functional theory (DFT) calculations revealed that the high FE and current density were attributed to the specific interaction between Ag nanoparticles and the surface modification by the anchoring agent, which provided more active sites for the CO_2RR. In addition, Ag catalysts with well-designed morphologies can also improve the catalytic activity for CO selection.[29,30] Voiry *et al.*[30] prepared a superstructural Ag catalyst *via* assembling two-dimensional Ag nanoprisms. The vertically stacked Ag nanoprisms exposed more than 95% of the edge sites, leading to an increased activity for CO_2-to-CO electroreduction and exhibiting a high CO FE of 96.3% at −0.6 V *vs.* RHE (Table 1). Sun *et al.*[31] synthesized 3D porous Ag nanostructures *via in situ* electroreduction of Ag benzenethiolate nanoboxes. The as-prepared porous Ag nanostructures exhibited high catalytic performance because of the abundant active sites, which resulted from the 3D hierarchical channels in the porous structures. The crystal facets of Ag also have a crucial impact on the activity and selectivity for the CO_2RR. Generally, Ag(110) shows higher catalytic activity for CO_2-to-CO conversion than Ag(111) or Ag(100).[32,33] The DFT simulations revealed that the initial proton-coupled electron transfer for *COOH on the Ag(110) facet possessed a lower activation energy barrier than that on Ag(111) or Ag(100), leading to enhanced CO_2RR performance.[34]

Molecular catalysts have also been evaluated as CO_2-to-CO catalysts because of their unique adjustable structures toward improved performance.[35] Porphyrins and phthalocyanines are the most studied catalysts and have been widely used for the electrochemical CO_2RR. Berlinguette *et al.*[36] used a commercially available cobalt phthalocyanine (CoPc) as the electrocatalyst in a zero-gap membrane flow cell for the electrochemical CO_2RR. A high selectivity of CO (>95%) could be achieved at a current density of 150 mA cm^{-2} with continuous long-term (more than 100 hours) operation, demonstrating molecular catalysts to be promising candidates for industrial CO_2-to-CO conversion. However, molecular catalysts tend to suffer from poor electroconductivity and stability issues. Immobilizing molecular catalysts on carbonaceous supports such as carbon nanotubes (CNTs),[37] carbon black (CB),[38] and carbon paper (CP)[39] can be an effective method to improve the

Table 1 Representative catalysts for electroreduction of CO_2 to CO

Catalyst	Catalyst type	Potential (V *vs.* RHE)	Partial current density (mA cm^{-2})	Electrolyte	FE (%)	Ref.
Tri-Ag-NPs	Ag-based nanoparticles	−0.86	~1	0.1 M $KHCO_3$	96.8	29
2D Ag-NPs	Ag-based nanoparticles	−0.6	3.89	0.1 M KOH	96.3	30
3D porous Ag	Ag-based nanoparticles	−1.03	6	0.1 M $KHCO_3$	96	31
PON-Ag	Ag-based nanoparticles	−0.69	4.4	0.5 M $KHCO_3$	96.7	33
CoPc/CNT-MD	Molecular catalyst	−0.9	~35	0.5 M $KHCO_3$	97	37
CoPc/CB	Molecular catalyst	−0.68	18.1	0.5 M $KHCO_3$	93	38
CoPP@CNT	Molecular catalyst	−0.6	25.1	0.5 M $KHCO_3$	98.3	43
CoTMAPc@CNT	Molecular catalyst	−0.72	~20	0.5 M $KHCO_3$	99	45
Ni-SAC@NCs	SAC	−0.6	~10	0.5 M $KHCO_3$	95	50
FeN_5	SAC	−0.46	2	0.1 M $KHCO_3$	97	51
$Zn–N_4$	SAC	−0.43	4.8	0.5 M $KHCO_3$	95	54
Co–Tpy–C	SAC	−0.8	6	0.5 M $NaClO_4$	98	55

current density and stability. The supports with high surface area, high conductivity, and catalytic inertness are conducive, as otherwise, they could interfere with the CO_2RR.[40–42] Zhao *et al.*[37] dispersed CoPc on CNTs *via* π–π stacking interactions, achieving an FE_{CO} of 97% at 200 mA cm^{-2}. In addition, the molecularly dispersed CoPc on CNTs presented higher catalytic activity and stability than the aggregated one.[37] Covalent grafting is another effective method for the immobilization of molecular catalysts. For example, Han *et al.*[43] covalently grafted cobalt porphyrin (CoPP) onto the surface of CNTs by reacting protoporphyrin IX cobalt chloride with hydroxyl-functionalized CNTs. This method enabled high catalyst loading in a better dispersion, achieving a high FE_{CO} of 98.3% at −0.65 V *vs.* RHE. Compared to non-covalent bonding, the covalent grafting method is more practical in stabilizing ionic molecular catalysts. For example, molecules with positively charged groups have shown higher CO_2RR activity than those with the neutral counterparts.[38,44] However, the presence of multiple ionic groups in the molecular catalysts may lead to poor stability because of the increased water solubility. To address this issue, Ye *et al.*[45] covalently grafted a molecular catalyst onto CNTs *via* an *in situ* functionalization strategy to improve the stability. Cobalt tetraamino phthalocyanine (CoTAPc) was firstly covalently grafted on CNTs *via* a diazo-reaction, and then methylated to form cobalt tetra-(4-*N*,*N*,*N*-trimethylanilinium) phthalocyanine (CoTMAPc). A stable current density of 239 mA cm^{-2} and high FE_{CO} of 95.6% were obtained in a flow cell at −0.7 V *vs.* RHE.[45] Another strategy to stabilize molecular catalysts is by forming a layered structure such as an ultrathin metal–organic framework or covalent organic framework, in which the metal complexes will be arranged in a co-planar configuration to avoid aggregation.[46] In addition, fixing the metal complexes in the framework can also mitigate the leaching of catalysts.[47]

Single-atom catalysts (SACs) have attracted increasing attention for the electrochemical CO_2RR, because of their high atom utilization efficiency and tunable activities. Metal centers are important factors for the catalytic performance of SACs. Generally, Ni and Fe-based SACs are highly active for CO production.[48,49] Jiang *et al.*[48] prepared a series of single-atom metals implanted in N-doped carbon (M–N–C; M = Fe, Co, Ni, and Cu) for CO_2-to-CO conversion. The results showed that Ni–N–C and Fe–N–C had much lower energy barriers for *COOH formation than Co–N–C and Cu–N–C (Fig. 3a), indicating higher catalytic activity of Ni and Fe SACs. In addition, the limiting potential difference between the CO_2RR and hydrogen evolution reaction ($U_L(CO_2) - U_L(H_2)$) was also evaluated for CO selectivity, and Ni–N–C showed a more positive value (Fig. 3b), representing higher CO_2RR selectivity than hydrogen evolution. Zhou *et al.*[50] recently prepared N-doped carbon-supported Ni SACs (Ni-SAC@NCs) as electrocatalysts for CO_2-to-CO conversion. The as-prepared Ni-SAC@NCs could achieve a high FE_{CO} of 95% at −0.6 V *vs.* RHE and keep over 80% FE in a wide potential window (−0.6 to −0.9 V *vs.* RHE). Wang *et al.*[51] synthesized singly dispersed FeN_5 active sites supported on N-doped graphene with an additional axial ligand coordinated to FeN_4 *via* thermal pyrolysis of hemin and melamine molecules on graphene (Fig. 3c). The FeN_5 SAC exhibited a high FE_{CO} of 97% at −0.46 V *vs.* RHE (Fig. 3d). DFT calculations showed that the weak binding strength of *CO to the FeN_5 site promoted the desorption of CO, thus resulting in higher CO selectivity than in the case of FeN_4 (Fig. 3e).[51] In addition, Ni-based SACs usually present higher catalytic activity and improved partial current density compared to Fe-based ones, as the $Fe–N_x$ site possessed strong binding of *CO.[52] Zn- and Co-based SACs have a higher activation barrier for CO_2-to-CO electrolysis and show poorer activity than the Ni and Fe-based SACs.[22,53] Xu *et al.*[54] prepared a N-anchored Zn SAC supported on carbon (ZnN_x/C) for CO formation. The as-prepared ZnN_x/C electrocatalyst showed a high catalytic selectivity with an FE_{CO} of 95% at −0.43 V *vs.* RHE. DFT calculations demonstrated that the four-N-anchored Zn active sites ($Zn–N_4$) could reduce the energy barrier for the formation of *COOH, leading to high catalytic activity for CO selection. Kang *et al.*[55] synthesized a series of Co SACs (Co–Tpy–C) by pyrolysis of a Co terpyridine organometallic complex at different temperatures. The Co–Tpy–C electrocatalyst showed excellent catalytic performance for CO formation with over 95% FE in a wide potential window (−0.7 to −1.0 V *vs.* RHE). Regulating the coordination environment of SACs can be an effective approach to improve the CO_2-to-CO electroreduction

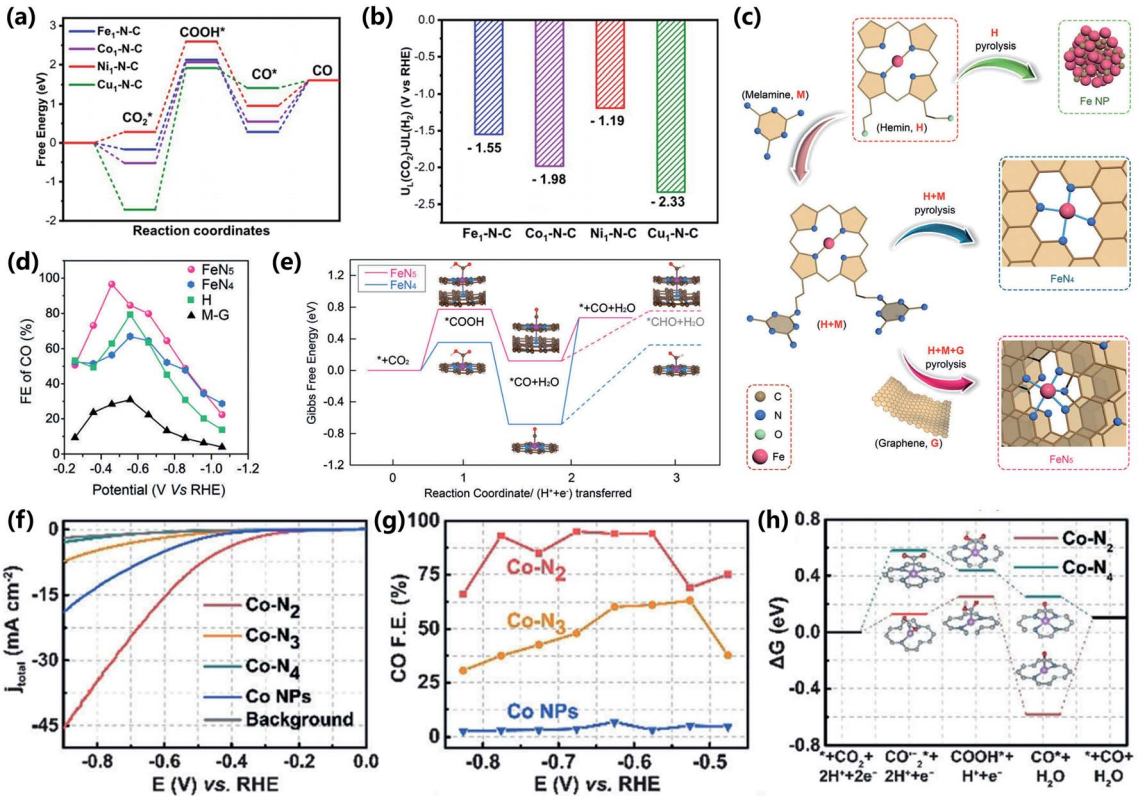

Fig. 3 (a) Free energy diagrams of CO_2 reduction to CO on M–N–C; M = Fe, Co, Ni, and Cu. (b) The values of $U_L(CO_2) - U_L(H_2)$ for M–N–C. Adapted with permission.[48] Copyright 2020, Wiley-VCH. (c) Synthetic route towards single-atom FeN_4 and FeN_5 catalysts. (d) FE_{CO} of FeN_4 and FeN_5 catalysts at different potentials. (e) Free energy profile with the optimized intermediates of CO_2 reduction to CO on FeN_4 and FeN_5 catalysts. Adapted with permission.[51] Copyright 2019, Wiley-VCH. (f) LSV of Co–N_2, Co–N_3, Co–N_4, and Co NPs and pure carbon. (g) CO FEs at different applied potentials of Co–N_2, Co–N_3, and Co NPs. (h) Gibbs free energy diagrams of electroreduction to CO on Co–N_2 and Co–N_4. Adapted with permission.[56] Copyright 2018, Wiley-VCH.

performance.[56–58] For example, Co SACs with different nitrogen coordination numbers showed different catalytic performance for the CO_2RR towards CO production.[56] A Co SAC with two coordinated nitrogens (Co–N_2) presented higher catalytic activity than the Co SAC with four coordinated nitrogens (Co–N_4), achieving FE_{CO} of 94% at −0.63 V *vs.* RHE with a current density of 18.1 mA cm^{-2} (Fig. 3f–h). The reduced nitrogen coordination number led to extra vacant 3d orbitals of Co atoms that might be beneficial for CO_2 reduction.

2.2 Formate/formic acid

Formate/formic acid ($HCOO^-$/HCOOH) is a valuable chemical ingredient employed in various industries, and its consumption has expanded significantly over the last several years.[59] p-Block metals, such as Sn, In, Bi, and Pd, and their composites, present a high selectivity for $HCOO^-$/HCOOH.[23] Sn is among the most widely employed metals for HCOOH electrocatalysis. Jaramillo *et al.*[60] presented a volcano plot (Fig. 4a) for $HCOO^-$ partial current density using *OCHO binding energy as a descriptor. Sn was at the saddle point of the volcano curve, indicating the optimal lowest *OCHO binding energy of Sn and thus the highest HCOOH selectivity.[60] Both Sn metal and Sn oxides display remarkable catalytic activity for CO_2-to-HCOOH conversion. Sn^{IV}, in particular, can efficiently minimize the CO_2 reduction overpotential by reducing the energy barriers of HCOOH formation. Meanwhile, Sn^{II} helps to increase selectivity toward HCOOH production by increasing the energy barriers for H_2 and CO generation according to the DFT calculations.[61] Multivalent Sn species exhibit higher catalytic activity than Sn or Sn oxides. Kang *et al.*[62] *in situ* constructed SnO_2/Sn heterostructures on the surface of SnO_2 nanoparticles, which exhibit higher FE_{HCOOH} of 93% at −1.0 V *vs.* RHE (Table 2) than pristine SnO_2 and Sn. A series of Sn/SnO/SnO_2 nanosheets were also reported, exhibiting a high FE_{HCOOH} of 89.6% at −0.9 V *vs.* RHE.[63] Theoretical simulations demonstrated that multivalent Sn species synergistically accelerated CO_2 activation, *OCHO adsorption, and electron transfer, resulting in a higher reduction rate of Sn/SnO/SnO_2.[63] Moreover, the morphologies and structures of SnO_x also influence the reduction activity.[64–66] A wavy structural SnO_2 network (Fig. 4b) showed a higher catalytic performance than commercial SnO_2 nanoparticles, with FE_{HCOOH} of 87.4% and current density of 22 mA cm^{-2} at an applied potential of −1.0 V *vs.* RHE.[65] Ultrathin SnO_2 quantum wires also exhibited enhanced current density and improved FE compared to SnO_2 nanoparticles because of the abundant grain boundaries as active sites on the surface.[64]

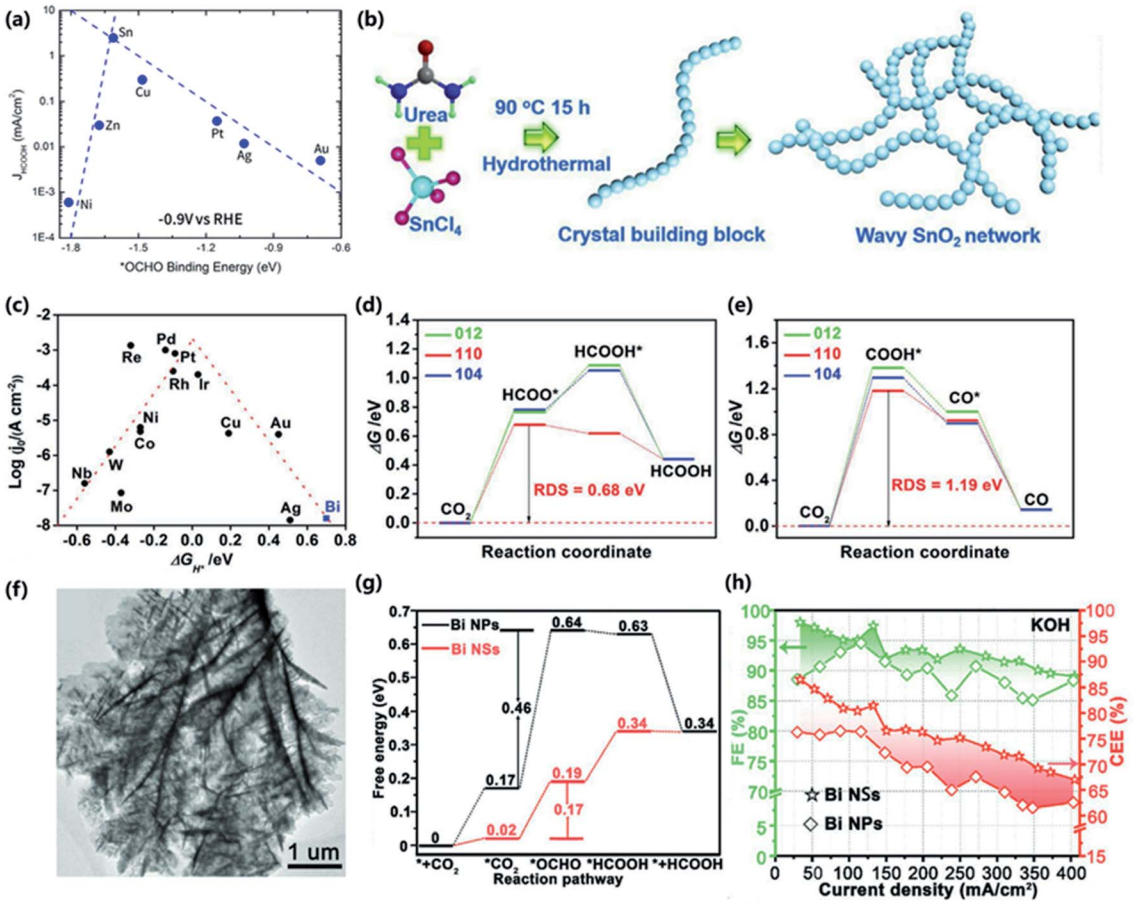

Fig. 4 (a) Volcano plot using *OCHO binding energy as a descriptor for $HCOO^-$ partial current density at −0.9 V *vs.* RHE. Adapted with permission.[60] Copyright 2017, the American Chemical Society. (b) Synthetic process towards NW-SnO_2. Adapted with permission.[65] Copyright 2020, Elsevier. (c) Volcano plots of j_0 as a function of the ΔG_{H^*} for Bi and other catalysts. (d) Gibbs free energy diagrams of Bi for the reduction of CO_2 into HCOOH. (e) Gibbs free energy diagrams of Bi for the reduction of CO_2 into CO. Adapted with permission.[67] Copyright 2020, Wiley-VCH. (f) TEM image of Bi NSs. (g) Gibbs free energy profiles for CO_2 electroreduction to HCOOH on Bi NPs and Bi NSs. (h) FEs and CEEs of formic acid over two electrocatalysts in 1 M KOH. Adapted with permission.[68] Copyright 2020, Wiley-VCH.

Bi also presents good $HCOO^-$/HCOOH production selectivity and high catalytic stability for CO_2 electrocatalytic reduction. Jiang *et al.*[67] demonstrated a volcano plot of j_0 as a function of the ΔG_{H^*} for Bi and other catalysts (Fig. 4c). Bi appeared at the bottom corner point of the volcano plot, which indicated the poor HER performance of Bi and the possibility for high CO_2RR activity.[67] The free energy calculations (Fig. 4d and e) revealed that HCOOH generation was more favorable than CO

Table 2 Representative catalysts for electroreduction of CO_2 to HCOOH

Catalyst	Catalyst type	Potential (V *vs.* RHE)	Partial current density (mA cm^{-2})	Electrolyte	FE (%)	Ref.
Sn foil	Metal Sn	−0.9	—	0.1 M $KHCO_3$	70	60
SnO_2/Sn	Sn oxides	−1.0	28.7	0.5 M $KHCO_3$	93	62
Sn/SnO/SnO_2	Sn oxides	−0.9	~20	0.5 M $KHCO_3$	89.6	63
Sub-2 nm SnO_2 QWs	Sn-based nanoparticles	−8.2	~11	0.1 M $KHCO_3$	87.3	64
NW-SnO_2	Sn-based nanoparticles	−1.0	22	0.5 M $KHCO_3$	87.4	65
DEA–SnO_x/C	Sn-based nanoparticles	−7.5	6.7	0.5 M $KHCO_3$	84.2	66
Bi/rGO	Metal Bi	−0.8	—	0.1 M $KHCO_3$	98	67
Bi NTs	Bi-based nanoparticles	−1.0	~30	0.5 M $KHCO_3$	97	69
Bi_2O_3NSs@MCCM	Bi oxides	−1.26	17.7	0.1 M $KHCO_3$	93.8	71
Bi_2O_3-NGQDs	Bi oxides	−1.0	22	0.5 M $KHCO_3$	95	72
Bi–Sn aerogel	Bimetal	−1.0	10	0.1 M $KHCO_3$	93.9	73
Bi–SnO/Cu foam	Bimetal	−1.7 *vs.* Ag/AgCl	12	0.1 M $KHCO_3$	93	74
$In_{1.5}Cu_{0.5}$ NPs	Bimetal	−1.2	8	0.1 M $KHCO_3$	90	77
$Zn_{0.95}In_{0.05}$	Bimetal	−1.2	22	0.5 M $KHCO_3$	95	78

generation, attributed to the lower ΔG_{RDS}.[67] Furthermore, Bi catalysts with varying surface structures exhibit different catalytic capabilities. A series of Bi nanosheets with flat surfaces (Bi NSs) and Bi nanotubes with surface curvatures (Bi NTs) were manufactured to investigate the electrochemical CO_2-to-HCOOH performance.[69] Bi NTs acquired a maximum FE_{HCOOH} of 97% at −1.0 V *vs.* RHE and a wide potential window of over 80% FE, which was superior to that of Bi NSs and Bi bulk powder.[69] DFT simulations revealed that the higher $*CO_2$ absorption near the curved Bi NT surfaces minimized the energy barrier for CO_2 reduction to HCOOH.[69] Wu *et al.*[68] constructed leafy structural Bi NSs (Fig. 4f) by *in situ* electroreduction of the Bi-based metal–organic framework CAU-17. The leafy structure with abundant Bi/Bi–O active sites reduced the free energy barrier for $*CO_2$ to *OCHO from 0.46 eV to 0.17 eV (Fig. 4g), resulting in remarkable HCOOH formation performance (>200 mA cm^{-2}, >90% FE, Fig. 4h).[68] Bi oxides also exhibit excellent catalytic performance towards HCOOH formation.[70–72] For example, immobilizing Bi_2O_3 nanosheets on a multi-channel carbon matrix (Bi_2O_3NSs@MCCM) could afford a maximum FE of 93.8% at −1.26 V *vs.* RHE with a corresponding current density of 17.7 mA cm^{-2}.[71] The interwoven MCCM with faster electron transport and the ultrathin Bi_2O_3 nanosheets with ample active sites simultaneously enabled high FE (>90%) to be obtained in a broad potential window.[71]

Constructing bimetallic electrocatalysts is also an effective strategy for improving the HCOOH electrosynthesis. A three-dimensional porous Bi–Sn bimetallic aerogel exhibited superior catalytic performance to Bi and Sn, with a high FE_{HCOOH} of 93.9% at −1.0 V *vs.* RHE.[73] The as-prepared aerogel established more active sites because of the interconnected channels and abundant interfaces.[73] DFT calculations demonstrated that the coexistence of Bi and Sn lowered the energy barrier for the synthesis of HCOOH, resulting in improved catalytic activity.[73] Guan *et al.*[74] used Cu foam as the substrate to grow Bi-doped SnO nanosheets, forming a Bi–SnO/Cu foam electrode. Bi doping strengthened the selectivity of HCOOH by enhancing the adsorption capacity of the SnO(001) facet for *OCHO intermediates *via* electron orbital hybridization.[74] Furthermore, electrons were transferred from the electrocatalyst to the Cu foam, which favored the adsorption of *OCHO intermediates by maintaining Sn in a positive oxidation state.[74] A series of Bi/CeO_x catalysts were prepared, exhibiting high production rate (2600 μmol h^{-1} cm^{-2}) and FE (92%) at high current density (149 mA cm^{-2}).[75] The enhanced performance of Bi/CeO_x was attributed to its larger electrochemically active surface area (ECSA), plentiful catalytically active sites, facilitated CO_2 adsorption and activation, faster charge transfer, and reaction intermediate stability by the supporting amorphous CeO_x matrix.[75] Heterostructured intermetallic CuSn electrocatalysts (Cu_3Sn/Cu_6Sn_5) supported on porous copper foam demonstrated an FE of 82% and a current density of 18.9 mA cm^{-2} at −1.0 V *vs.* RHE.[76] Theoretical calculations revealed that the high catalytic activity was primarily due to the interfaces between the Cu_6Sn_5 and Cu_3Sn intermetallics, where the adsorption of the *OCHO intermediate was stronger than that of *COOH. The free energy of adsorbed hydrogen was also upshifted, leading to the suppression of the HER and the selective production of HCOOH.[76] Bimetallic In_xCu_y (x and y are the molar ratio) nanoparticle (NP) electrocatalysts, with different growth directions of crystal facets with varying In/Cu ratios, realized 90% FE at −1.2 V *vs.* RHE.[77] DFT calculations further revealed that the In(101) facet of In_xCu_y NPs stabilized the *OCHO intermediate more effectively, thereby reducing the potential barrier for CO_2 to HCOOH conversion.[77] In–Zn bimetallic nanocrystals outperformed In NCs because of the In–Zn interfacial sites, with a high FE of 95% and a formation rate of 0.40 mmol h^{-1} cm^{-2} at −1.2 V *vs.* RHE.[78]

2.3 Methane

Electroreduction of CO_2 to CH_4 is more economically advantageous, considering that CH_4 has the highest gravimetric energy density (13.9 kW h kg^{-1}) among all the hydrocarbon compounds and has been utilized as an alternative energy carrier to replace traditional fossil fuels.[79] However, the electroreduction process is more difficult because of the eight-electron step, which requires a higher overpotential.

Cu-based heterogeneous catalysts have attracted considerable attention due to their propensity to produce multi-electron transfer products. They are considered one of the most promising candidates for electroreduction of CO_2 to CH_4. For example, by employing electrodeposited Cu on carbon paper, Zhang *et al.*[80] achieved an FE for CH_4 formation of 85% with a partial current density of 38 mA cm^{-2} at −2.8 V *vs.* RHE (Table 3). Besides, the facet, size, and morphology of nanostructured Cu also influence the generation of the target products. It has been revealed that the Cu(111) surface is selective for CH_4, whereas the Cu(100) facet enhances C_2H_4 generation at low overpotentials.[81,82] A series of Cu spheres (Cu_{sph}), Cu cubes (Cu_{cub}) and Cu octahedra (Cu_{oh}) were synthesized according to colloidal methods.[83] The Cu_{cub} with the (100) facet was highly selective toward C_2H_4, while Cu_{oh} with the (111) facet preferred the production of CH_4. Buonsanti *et al.*[84] prepared different sized octahedral Cu(111) nanocrystals varying from 75 to 310 nm (Fig. 5a–c). The 75 nm Cu(111) octahedral nanocrystals showed the best performance with 55% FE for CH_4 at −1.25 V *vs.* RHE (Fig. 5d). Moreover, forming a core–shell structure with surface coating on Cu can further improve the selectivity towards CH_4 and stabilize the morphology during catalysis.[85,86] For example, Cu nanowire electrodes coated with polydopamine (PDA) showed 2.3 times higher CH_4 selectivity and catalytic stability, compared with the pristine Cu nanowires (Fig. 5e–h).[86] The amino groups of PDA facilitated the proton transfer from the bulk solution to the catalytic interface and the phenol hydroxyl tended to stabilize the *CO intermediates, promoting the formation of CH_4 on the Cu nanowire surface.

Alloying Cu with a second metal is another widely adopted way to improve CH_4 selectivity. A series of PdCu bimetallic catalysts with different structures were synthesized by adjusting the composition ratio.[87] In particular, the concave rhombic dodecahedral Cu_3Pd nanocrystals exhibited FE of 40% toward CH_4 at −1.2 V *vs.* RHE with enhanced CH_4 current density compared to Cu foil, resulting from the high-index facets and

Table 3 Representative catalysts for electroreduction of CO_2 to CH_4

Catalyst	Catalyst type	Potential (V *vs.* RHE)	Partial current density (mA cm^{-2})	Electrolyte	FE (100%)	Ref.
Cu–P-ED	Cu-based catalyst	−2.8	38	0.5 M $NaHCO_3$	81	80
Octahedral CuNCs	Cu-based catalyst	−1.25	—	0.1 M $KHCO_3$	55	84
Ultrathin CuNWs	Cu-based catalyst	−1.25	~8	0.1 M $KHCO_3$	55	85
CuNWs@PDA	Cu-based catalyst	−0.93	—	0.5 M $KHCO_3$	29	86
Cu_3Pd	Bimetal	−1.2	~4	0.1 M $KHCO_3$	40.6	87
Cu/ZnO_x	Bimetal	−1.1	~17	0.1 M $KHCO_3$	~36	88
CuAg	Bimetal	−1.17	—	0.1 M $KHCO_3$	72	89
CuAg thin film	Bimetal	−1.4	—	0.1 M $KHCO_3$	59.3	90
AgCo	Bimetal	−2	—	0.5 M KHCO3	19.5	91
Cu–N–C-900	SAC	−1.6	14.8	0.1 M $KHCO_3$	38.6	92
CuN_2O_2	SAC	−1.44	~30	0.5 M $KHCO_3$	78	93
Fe–N–C SAC	SAC	−1.8	31.8	1 M $KHCO_3$	85	96
Cu-3TPyP	SAC	−1.0	—	1 M KOH	62.4	103
g-C_3N_4	Metal-free catalyst	−1.27	14.8	0.5 M $KHCO_3$	44	99
EDTA@CNT	Metal-free catalyst	−1.3	16.5	0.5 M $KHCO_3$	61.6	102

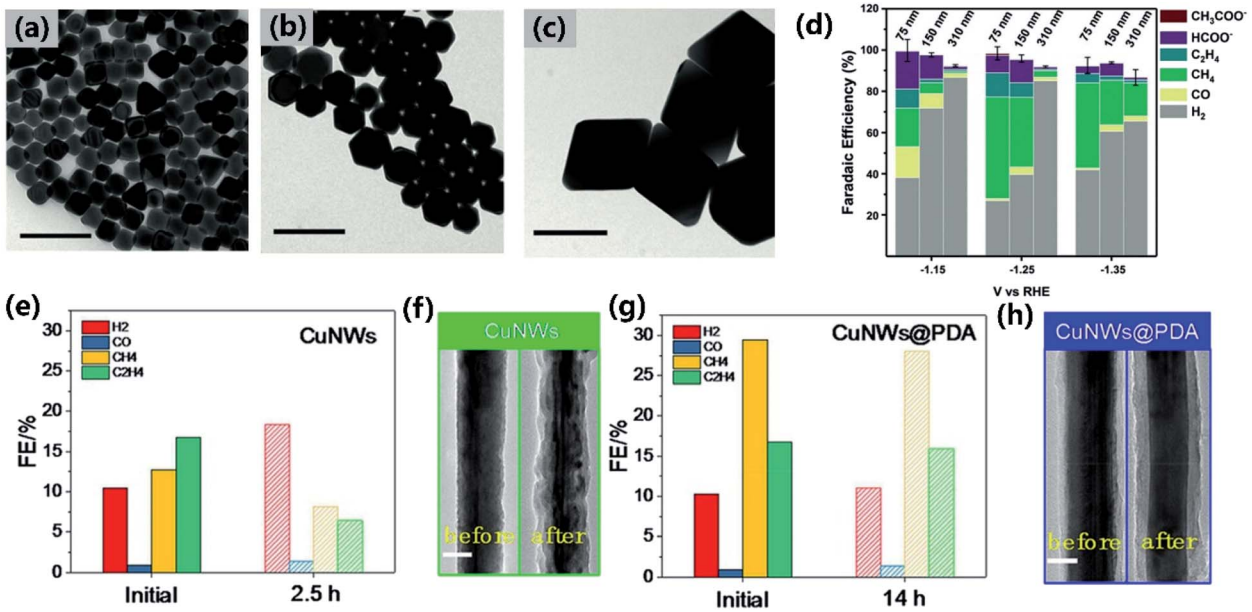

Fig. 5 (a–c) TEM images of the 75 nm, 150 nm, and 310 nm Cu_{oh}-NCs. Scale bars are 300 nm. (d) FEs of the three sizes of Cu_{oh}-NCs with a loading of 11 mg cm^{-2} on glassy carbon plates measured in CO_2-saturated 0.1 M $KHCO_3$ at different potentials. Adapted with permission.[84] Copyright 2020, American Chemical Society. (e) The FEs for Cu nanowires at the initial and final stages of electrocatalysis. (f) TEM images of Cu nanowires before and after 1 h electroreduction. (g) The FEs for Cu nanowires@PDA at the initial and final stages of electrocatalysis. (h) TEM images of Cu nanowires@PDA before and after 1 h electroreduction. Adapted with permission.[86] Copyright 2018, Wiley-VCH.

alloying effect. Cu/ZnO_x nanoparticles, constructed by magnetron sputtering and subsequent oxidation–reduction treatment, exhibited a maximum FE of ~36% at −1.1 V *vs.* RHE and a long-term durability for electroreduction to CH_4 due to the active sites at the Cu/ZnO_x interface.[88] Huang *et al.*[89] established an intimate atomic CuAg interface on the surface of Cu nanowires, achieving a maximum FE of 72% towards CH_4 generation at −1.17 V *vs.* RHE. Recently, an oxidation-resistive CuAg thin film was reported, which electroreduced preferentially to CH_4 (FE of 59.3%) at −1.4 V *vs.* RHE.[90] Despite the majority of the alloys for CH_4 production being Cu-based, some alloys without Cu were also reported. For example, Verma *et al.*[91] prepared a bimetallic AgCo electrocatalyst by simultaneously reducing $Co(NO_3)_2$ and $AgNO_3$ with sodium borohydride. The maximum FE observed for CH_4 was 19.5% at −2.0 V *vs.* RHE.

SACs have also been evaluated as heterogeneous catalysts for electrochemical CH_4 selection because of their unique electrical characteristics and maximized atomic usage. A series of single-atom Cu catalysts distributed on nitrogen-doped carbon were prepared by changing the pyrolysis temperature and the N coordination conditions. The highest CH_4 FE was 38.6% at −1.6 V *vs.* RHE with a partial current density of 14.8 mA cm^{-2}.[92] DFT simulations further indicated that high Cu concentration with nearby Cu–N_2 sites was more favorable for the C_2H_4

generation owing to the reduced free energy for C–C coupling, whereas the isolated Cu–N_4, the neighboring Cu–N_4, and the isolated Cu–N_2 were all prone to yield CH_4.[92] A carbon-dots-based CuN_2O_2 SAC was synthesized with remarkably high FE (78%) and high partial current density of 40 mA cm^{-2}.[93] The introduction of oxygen ligands provided a new electronic structure, leading to lower required energy for the limiting step to form CH_4.[93] Ultrathin porous Al_2O_3 with enriched Lewis acid sites was explored as an anchor for Cu single atoms to catalyze electrochemical CO_2 methanation, showing the FE for CH_4 approaching 62% at −1.2 V *vs.* RHE with the corresponding current density of 94.8 mA cm^{-2}.[94] Theoretical calculations suggested that Lewis acid sites in metal oxides could promote CO_2 methanation by optimizing intermediate adsorption. In addition, non-Cu-based SACs for CH_4 production have also been investigated.[95,96] For example, Zn SACs dispersed onto microporous N-doped carbon exhibited a high CH_4 FE of 85% at −1.8 V *vs.* SCE with a corresponding partial current density of 31.8 mA cm^{-2}.[96] Theoretical calculations revealed that for Zn SACs, the O atom rather than the C atom in the *OCHO intermediate preferred to form a chemical bond with Zn, blocking the generation of CO and helping to produce CH_4. Moreover, inspired by the bimetallic alloy catalysts, dual-atom catalysts (DACs), such as CuCr/C_2N[97] and N6V4–AgCr,[98] have been investigated for electrochemical reduction toward CH_4. They showed an extremely low overpotential due to the multiple active centers.

Metal-free catalysts, such as graphitic C_3N_4 (g-C_3N_4),[99] borophene,[100] graphene quantum dots (GQDs),[101] and ethylenediaminetetraacetic acid (EDTA),[102] have also been studied for electroreduction of CO_2 to CH_4. For example, Chen *et al.* reported that EDTA immobilized on CNTs showed a high FE of 61.6% toward CH_4 at −1.3 V *vs.* RHE with a partial current density of 16.5 mA cm^{-2}, competing with state-of-the-art Cu-based catalysts. The Lewis basic COO^- groups in the EDTA molecule were suggested to be the active sites for CO_2 reduction.

2.4 Methanol

Methanol is an important commodity chemical in industry. It can be used as clean fuel directly due to its high energy density and stable storage properties. Besides, CH_3OH can also be used as a feedstock to produce liquid fuels such as dimethyl ether (DME), synthetic gasoline, and several organic compounds.[104] Currently, most of the commercial CH_3OH is produced from syngas (the mixture of CO and H_2) under high temperature (250–300 °C) and pressure (3.5–10 MPa), which usually requires high-security equipment.[105] Electrochemical reduction of CO_2 to CH_3OH provides a new platform to produce CH_3OH under ambient conditions.

Compared with CO and HCOOH, the transformation of CO_2 to CH_3OH requires six electrons, so the reduction reaction is considered kinetically slow. Among the studied materials, Cu and Pd, as well as their mixtures and oxidized forms, have been reported to be the most active materials for the electrochemical transformation of CO_2 to CH_3OH.[106,107] Flake *et al.*[108] demonstrated that Cu_2O electrodes showed a remarkably higher CH_3OH yield rate (43 μmol cm^{-2} h^{-1}) and FE (38%) than air-oxidized or anodized Cu electrodes (CuO) (Table 4), suggesting that Cu^I species play a critical role in electrode activity and selectivity to CH_3OH. However, there are two shortcomings of the Cu_2O catalyst: (1) the current density is not high; (2) Cu_2O is not stable and it may be reduced to metallic Cu, resulting in the generation of side products. To solve these problems, many strategies have been proposed. For example, Cu_2O loaded on CNTs could increase the current density.[109] Supporting Cu_2O on the CNTs increased the active surface area and the accessibility of the reactants to the active sites because of the high length-to-diameter tubular structure of CNTs. The presence of the CNTs offered both reaction sites and electrons to increase the conversion rate of the intermediates to targeted multi-electron products.[109] In addition, mixing ZnO with Cu_2O (Cu_2O/ZnO) showed better stability (5 h) than pure Cu_2O (0.5 h).[110] It was proposed that ZnO strengthened the Cu–CO bond, increasing the selectivity to alcohols and stabilizing Cu in the hydrogenation reaction.[110] Besides, Cu_2O/ZnO-based gas-diffusion electrodes could solve the mass transfer problem and improve current density and stability.[111] A series of CuSe nanocatalysts were prepared for electrochemical reduction of CO_2 to CH_3OH using 1-butyl-3-methylimidazolium tetrafluoroborate ([Bmim]BF_4) aqueous solution as electrolyte.[112] The as-prepared $Cu_{1.63}Se(1/3)$ nanocatalysts presented a high FE of 77.6% at a low overpotential of 285 mV with a current density of 41.5 mA cm^{-2}. The usage of ionic liquid enhanced the mass transport of CO_2 to the catalyst surface, accelerating the formation of crucial *CO species for CH_3OH production (Fig. 6a). Constructing bimetallic catalysts can be an effective way to improve the catalytic performance for CO_2-to-CH_3OH conversion. For example, nanostructured CuAu alloys showed 19 times higher FE than that on pure Cu because of the multifunctional catalysis of the alloys.[113] Han *et al.*[114] prepared PdCu bimetallic aerogels *via* a template-free self-assembly process, achieving a high FE of 80% at a very low overpotential (0.24 V). The amorphous Cu had large numbers of abundant defects as catalytic centers to enhance the CO_2RR. In addition, the Pd–Cu surface was beneficial for CO_2 chemical adsorption and subsequent hydrogenation. So the synergistic effect between Pd and Cu as well as the network structure of the aerogels improved the performance of CO_2-to-CH_3OH conversion. Well-designed morphologies and structures can also enhance the catalytic activity. Zheng *et al.* prepared 2D hierarchical Pd/SnO_2 nanosheets and achieved a high 54.8% at −0.24 V *vs.* RHE.[107] This kind of structure could promote the adsorption of CO_2 on Pd–O–Sn interfaces, leading to enhanced electrocatalytic selectivity and stability. Wang *et al.*[115] designed a hollow urchin-like structure of $Co(CO_3)_{0.5}(OH)\cdot 0.11H_2O$ (Fig. 6b) and obtained a high FE of 97% for CH_3OH selection. The hollow urchin-like structure enhanced the transfer of CO_2 and diffusion of the generated CH_3OH, promoting CO_2 electroreduction activity.

Molecular catalysts are another class of catalysts that can produce CH_3OH from CO_2 *via* the electrochemical method. Robert *et al.*[116] deposited CoPc onto CNTs, and found that at pH 13, the CoPc could reduce CO to methanol with an FE of 14.3%

Table 4 Representative catalysts for electroreduction of CO_2 to CH_3OH

Catalyst	Catalyst type	Potential (V *vs.* RHE)	Partial current density (mA cm^{-2})	Electrolyte	FE (100%)	Ref.
Cu_2O	Cu oxides	−1.1	~5	0.5 M $KHCO_3$	38	108
Cu_2O/CNTs	Cu oxides	−0.8	12	0.5 M $NaHCO_3$	38	109
Cu_2O/ZnO	Cu oxides	−1.3 (*vs.* Ag/Ag^+)	10	0.5 M $KHCO_3$	25	110
$Cu_{1.63}Se(1/3)$	Bimetal	−2.1 (*vs.* Ag/Ag^+)	41.5	$[Bmim]PF_6/CH_3CN/H_2O$ (5 wt%)	77.6	112
$Pd_{83}Cu_{17}$	Bimetal	−2.1 (*vs.* Ag/Ag^+)	31.8	$[Bmim]BF_4/H_2O$	80	114
Pd/SnO_2	Bimetal	−0.24	54.8	0.1 M $NaHCO_3$	54.8	107
$Co(CO_3)_{0.5}(OH)\cdot 0.11H_2O$	Morphology change	−0.98 (*vs.* SCE)	—	0.1 M $NaHCO_3$	97	115
CoPc/CNR	Molecular catalyst	−0.64	2.91	0.5 M $KHCO_3$	14.3	116
CoTAPc/CNT	Molecular catalyst	−1.0	10	0.5 M $KHCO_3$	28	117
Co-corrole	Molecular catalyst	−0.64	—	0.1 M phosphate	43	118

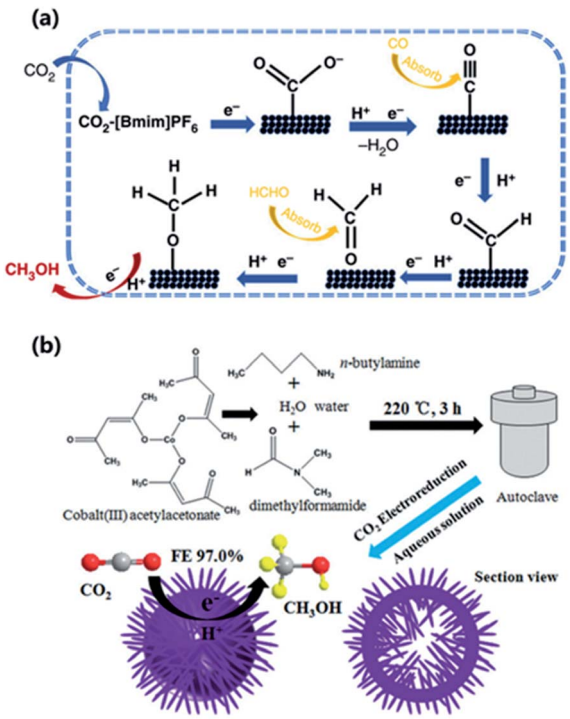

Fig. 6 (a) Mechanism study of CO_2 reduction to methanol in an ionic liquid. Adapted with permission.[112] Copyright 2019, Springer Nature. (b) Schematic of the synthesis of hollow urchin-like $Co(CO_3)_{0.5}(OH)\cdot 0.11H_2O$. Adapted with permission.[115] Copyright 2018, The Royal Society of Chemistry.

at −0.64 V *vs.* RHE. The pH had a significant effect in producing methanol; both acidic and highly basic solutions of pH 4 and 14 produced less methanol. The methanol selectivity decreased after long-term electrolysis, which was speculated to be due to the reduction of the C=N bond. In a similar study by Wang *et al.*,[117] highly dispersed CoPc on commercial CNTs (CoPc/CNT) also tuned the selectivity from CO to methanol. The production of methanol was proposed to go through a similar but not identical pathway, in which CO_2 was first reduced in a domino process to CO and further to methanol. Although the mechanism of the CNT induced effect was not clear, it was possible that the strong catalyst/CNT interaction played a critical role in tuning the electronic structure, as the dispersion of CoPc on other supports showed poor CO_2-to-methanol activity. Roy *et al.*[118] reported a cobalt(III) triphenylphosphine corrole complex (Co-corrole), which can reduce CO_2 to methanol (FE of 43% at −0.64 V *vs.* RHE) in 0.1 M phosphate buffer. Schöfberger *et al.*[119] also reported a similar structural Mn corrole complex (Mn-corrole), which can also electroreduce CO_2 to CH_3OH with a maximum FE of 19%. The corrole molecule seemed to make the radical intermediates more stable at the metal site, leading to the formation of multi-electron reduced products.[118]

2.5 C_{2+} products

Multicarbon (C_{2+}) products are more attractive than C_1 products due to their higher energy density as fuels and enhanced value as feedstocks in the chemical industry. So far, Cu and Cu-based compounds are the only metal materials explored to promote the CO_2RR to C_{2+} products with significant yields. Cu exhibits moderate binding energy for *CO, a crucial intermediate product involved in the C–C dimerization step.[120]

Cu species with controllable sizes and facets have been widely investigated to improve the catalytic activity towards C_{2+} selection. As discussed in the Methane section (Section 2.3), the Cu(111) facet is selective for CH_4. For other facets, Cu(100) enhances C_2H_4 generation and the Cu(110) facet favors C_2 oxygenate products like CH_3COOH, CH_3CHO, and C_2H_5OH.[121] A series of Cu_2O nanocrystals with different crystal facets were prepared for the electrochemical reduction of CO_2 to C_{2+} products.[122] The as-obtained concave octahedral Cu_2O with (511) high-index facets presented improved FE and increased current density for C_{2+} production compared to the dodecahedral Cu_2O with the (110) facet and cubic Cu_2O with the (100) facet, achieving the highest FE of 48.3% and partial current density of 17.7 mA cm^{-2} at −1.1 V *vs.* RHE. The well-maintained high-index facets and the active sites at the grain boundaries of the octahedral Cu_2O catalyst improved the C–C coupling reaction efficiency during the CO_2RR.[122] Besides the facets, well-designed morphologies can also enhance the catalytic performance. Sun *et al.*[123] reported Cu nanodendritic structures (Cu NDs) with a high ECSA (Fig. 7a). The abundant active sites facilitated electron transport and the C–C coupling reaction between *CO intermediates, leading to approximately 70–120% higher C_2H_4 generation than the the initial Cu particles (Fig. 7b). Yang *et al.*[124] prepared mesoporous Cu nanoribbons

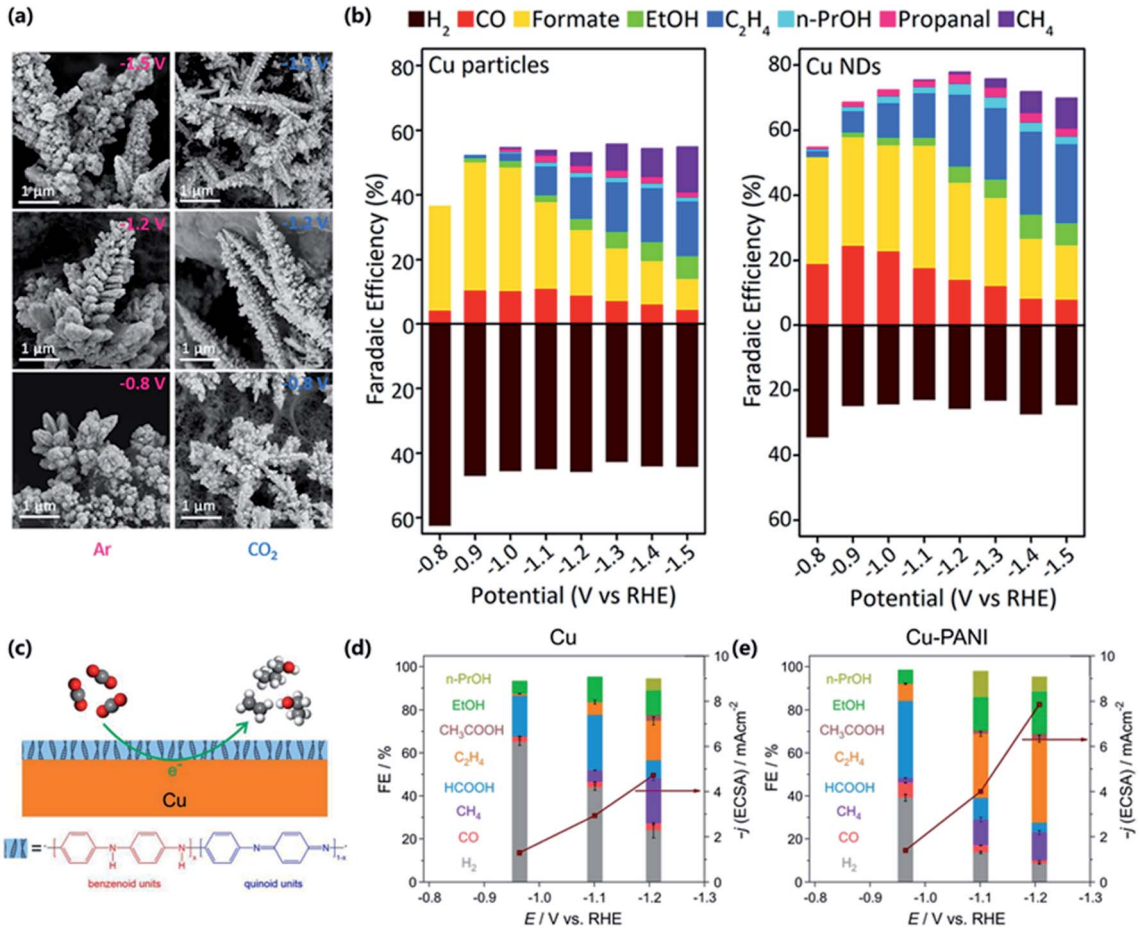

Fig. 7 (a) SEM images of Cu NDs at specific applied potentials after potentiostatic electrolysis for 20 min. (b) Faradaic efficiencies for the CO_2RR of the Cu particles (left) and the Cu NDs (right). Adapted with permission.[123] Copyright 2020, American Chemical Society. (c) Schematic diagram of the CO_2RR occurring at the Cu/PANI interface. (d) FE for every product and ECSA-normalized current density for the Cu. (e) FE for every product and ECSA-normalized current density for the Cu/PANI. Adapted with permission.[125] Copyright 2020, American Chemical Society.

via in situ electrochemical reduction of Cu-MOFs. The mesoporous structure of Cu nanoribbons could concentrate OH^- on the surface, which increased the local pH and led to improved selectivity of C_{2+} products.

The chemical state of Cu is another important parameter for the CO_2RR to C_{2+} products. During the electroreduction process, the electrodes tend to be reduced to Cu^0, regardless of the initial states. The peroxidation of Cu generally shows excellent selectivity toward C_{2+} products.[126,127] Han *et al.*[128] prepared two Cu-based electrodes with mixed oxidation states, HQ–Cu (containing Cu, Cu_2O, and CuO) and AN–Cu (containing Cu and $Cu(OH)_2$), to investigate the origin of the superior performance in oxide-/hydroxide-derived Cu. The results showed that the oxide crystals in HQ–Cu and the hydroxide crystals in AN–Cu were all reduced and fragmented into small irregular Cu grains, which facilitated C–C coupling at the grain boundaries. A similar oxide-formation and reduction process of Cu foils in aqueous solutions of KCl, KBr, or KI was also reported to show high catalytic performance due to the high density of surface defect sites at the prepared Cu surface after electroreduction.[129] The coexistence of Cu^+ and Cu^0 species also shows better performance.[130–132] However, the active Cu^+ species were likely reduced under CO_2RR conditions. Yu *et al.*[133] prepared catalysts with a nanocavity confinement structure, stabilizing the Cu oxidation state. The as-designed Cu_2O with nanocavities presented C_{2+} generation with an FE of over 75% and a partial current density of 267 mA cm^{-2}.

Catalyst surface modification is another practical strategy to enhance the performance of the electrochemical CO_2RR. This strategy can tailor the microenvironments near the catalyst surface for target products. Wang *et al.*[134] modified Cu electrodes with a series of amino acids, including glycine, DL-alanine, DL-leucine, DL-tyrosine, DL-arginine, and DL-tryptophan. The results showed that Cu electrodes modified with all kinds of amino acids performed better in producing C_2H_4 than the bare Cu electrode.[134] Theoretical calculations revealed that the hydrogen bond formation between CHO* and $-NH_2$ stabilized the CHO*, resulting in the improved generation of C_{2+} products in the CO_2 electroreduction.[134] A Cu surface coated with polyaniline (PANI) film (Fig. 7c) demonstrated enhanced FE for C_{2+} hydrocarbons (60%) compared with pristine Cu (FE of 15%), as shown in Fig. 7d and e.[125] The superiority of the Cu/PANI was

attributed to the coverage of PANI on the Cu surface, which improved the adsorption of the *CO intermediate and thus facilitated the C–C coupling, as revealed by *in situ* infrared spectroscopy.[125] Inspired by the construction of gas-trapping cuticles on subaquatic spiders, a superhydrophobic dendritic Cu coated with long-chain alkanethiols was proposed to mimic this kind of structure for the CO_2RR.[135] The bionic hydrophobic electrode obtained a high FE of 56% for C_2H_4 and 17% for C_2H_5OH under neutral conditions, superior to that of a wettable cathode (FE of 9% for C_2H_4 and 4% for C_2H_5OH). The superiority was attributed to the concentrated gaseous CO_2 wrapped on the hydrophobic Cu surface, consequently improving CO_2 reduction selectivity.[135] Bell *et al.*[136] adjusted the microenvironments of a bare Cu surface using different cation- and anion-exchanging ionomer-layer stacks. The commercial anion-exchanging ionomer Sustainion could improve the CO_2 solubility because of the imidazolium groups with high CO_2 affinity.[137] The negatively charged Nafion resin was used as an anion exchanging ionomer, which led to the exclusion of anions (bicarbonates) and gathering of CO_2RR-produced OH^-, forming a high pH condition around the Cu surface. The increased CO_2 solubility and the increased local pH by the bilayers influenced the overall water concentration and the product selectivity.

Metal-free carbon-based catalysts have also been applied as electrocatalysts to convert CO_2 to C_2 products. Pure carbon materials are inactive for the CO_2RR because of the weak CO_2 adsorption ability and high energy barrier for CO_2 activation.[138] Incorporating heteroatoms (such as boron, nitrogen, and sulfur) into carbon composites is an effective way to increase CO_2 activation capability, which lowers the energy barrier for C–C coupling on carbon-based materials.[139] Ajayan *et al.*[140] prepared N-doped graphene quantum dots (NGQDs) *via in situ* N doping on an exfoliated graphene oxide (GO) precursor. The NGQDs demonstrated a high FE of 90% for the overall CO_2RR, with a major hydrocarbon product, C_2H_4 (a maximum FE of 31% at −0.75 V *vs.* RHE), and a major oxygenate component, C_2H_5OH (a maximum FE of 16% at −0.78 V *vs.* RHE).[140] The high performance of NGQDs was obtained by the introduction of the N atom into sp^2-bonded carbon frameworks and the unique nanostructure of doped zigzag edges, which offered active sites for adsorbing CO_2.[140,141] Yu *et al.*[142] proposed a nitrogen-doped nanodiamond/Si rod array (NDD/Si RA) cathode for electroreduction of CO_2, presenting a major product of CH_3COOH (FE of 91% in a wide potential window from −0.8 to −1.0 V *vs.* RHE). The excellent efficiency could be attributed to its large energy barrier for the HER and the abundant, highly active N–sp^3C species for the CO_2RR.[142] Furthermore, B- and N-co-doped nanodiamond (BND) was reported for improved selection of C_2H_5OH. The BND achieved a high C_2H_5OH FE of 93.2% at −1.0 V *vs.* RHE, attributed to the synergistic effect of B and N co-doping.[143] Apart from heteroatom doping, tailoring porous carbon textures, which provides more active sites for CO_2 capture and reduction, could be another promising way to improve the CO_2 reduction performance. For example, N-doped mesoporous carbon with ordered cylindrical channel structures had high selectivity and efficiency towards C_2H_5OH.[144,145] DFT simulations revealed that microporous structures with active N sites had fast charge transfer kinetics and large driving potentials, which were critical for enhancing C_2H_5OH production.[145]

In summary, catalysts have drawn the most intense research efforts in the last decade, resulting in fast advancements in CO_2RR performance. The selectivity and catalytic performance of catalysts are not only related to their inherent properties, but also depend on their structures and morphologies. Reducing the bulk metal to nano-sized and even atom-sized catalysts (SACs) can be an effective method to get more active sites for the CO_2RR. Constructing bimetallic catalysts can be another strategy to obtain highly active catalysts because of the synergistic effect. As for the molecular catalyst, in addition to the molecular structures, the immobilization and good dispersion on carbonaceous supports can improve the electrical conductivity and expose more active sites for the CO_2RR. Moreover, the development of metal-free catalysts is important to reduce the catalyst cost in industrial utilization.

3. Electrolyzer design

Conventional H-cell configurations are suitable for laboratory-scale screening of catalysts for the electrochemical CO_2RR. However, they are severely constrained by mass transport due to the low solubility of CO_2 in aqueous electrolytes. With the development of flow cell configurations, vapor-fed CO_2 electrolyzers provide a promising platform for the commercialization of the electrochemical CO_2RR to value-added chemicals and fuels.

3.1 Gas diffusion electrodes

The utilization of gas diffusion electrodes (GDEs) is especially paramount for vapor-fed CO_2 electrolyzers, which allow direct delivery of gaseous CO_2 reactants to the catalysts, optimizing the mass transport for the electroreduction of CO_2.[146] The structure of a GDE typically consists of a porous catalyst layer (CL) and a diffusion medium, which is a hydrophobic layer composed of a macroporous gas diffusion layer (GDL) and a microporous layer (MPL), as shown in Fig. 8a. The diffusion medium provides channels for CO_2 to reach the CL and simultaneously separates the electrolyte from the CO_2 feed, leading to highly efficient mass transport and enhanced current density for the CO_2RR.[147] The electrochemical reduction of CO_2 on GDEs is generally regarded to occur at a solid–liquid–gas triple-phase boundary (Fig. 8b). During the electrochemical CO_2RR, the electrolyte penetrates into the porous diffusion medium and provides protons or water molecules to the catalysts, forming the triple-phase boundary with the gaseous CO_2 at the surface of the catalysts for electroreduction. To stabilize the triple-phase boundary, it is essential to prevent flooding by the excessive penetration of electrolyte into the GDEs. Improving the hydrophobicity of the MPL by coating with hydrophobic polymers such as polytetrafluoroethylene (PTFE) is a common method. It is worth mentioning that appropriate loading (usually 5–20 wt%) of PTFE is a prerequisite, since excessive loading leads to a considerable loss in GDL electrical conductivity, whereas low PTFE content results in flooding

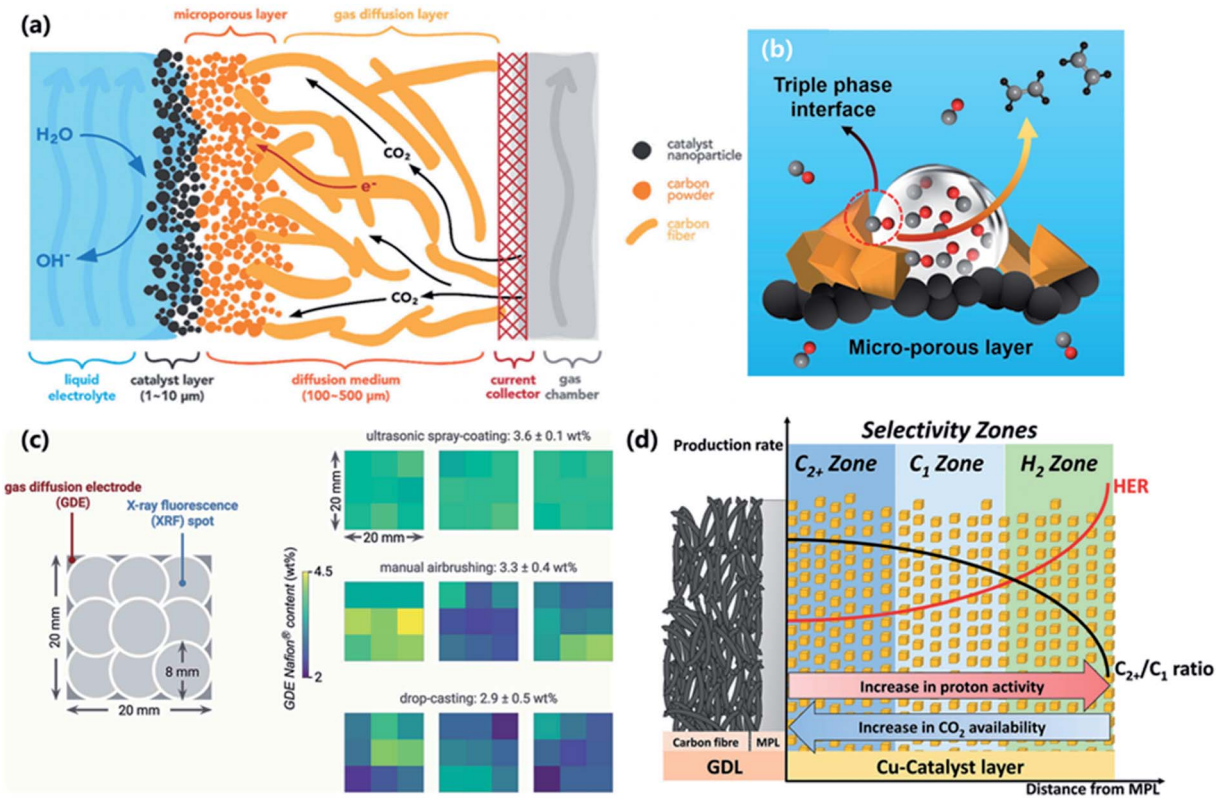

Fig. 8 (a) Schematic illustration of the gas diffusion electrode. Adapted with permission.[147] Copyright 2018, The Royal Society of Chemistry. (b) Schematic illustration of the solid–liquid–gas triple-phase boundary. Adapted with permission.[150] Copyright 2020, Wiley-VCH. (c) Nafion content measured by X-ray fluorescence (XRF) for GDEs prepared using ultrasonic spray-coating, manual airbrushing, and drop-casting. Adapted with permission.[151] Copyright 2020, The Royal Society of Chemistry. (d) Selectivity zones as a function of distance from the MPL substrate in the direction of the catholyte. Adapted with permission.[152] Copyright 2021, The Royal Society of Chemistry.

during long-term operation.[148] To further enhance the stability of GDEs at high current densities, modification of commercial GDEs with hydrophobic materials such as fluoroalkyl silane was performed, and the C_{2+} (mainly ethylene and ethanol) FE could remain at ~80% with stability for 40 hours at 400 mA cm^{-2} in 1.0 M KOH.[149]

Apart from the GDL parameters, the immobilization of catalysts on the GDL should also be addressed. The catalyst ink prepared from a mixture of ionomers and catalyst particles is deposited onto the GDL to form the CL. The ionomers act as both binders and ion conductors, establishing adhesion between the catalysts and the GDL to prevent the catalysts from shedding during the electroreduction. The ionomers are usually divided into cation exchange ionomers (CEIs) and anion exchange ionomers (AEIs) based on the functional groups in the polymer main chain. Although the ionomer is not directly engaged in the electroreduction process, the usage of different ionomers can change the microenvironments near the catalyst surface and influence the product selectivity of the electrochemical CO_2RR. Adjusting the microenvironments near the catalyst surface with bilayer AEI and CEI coatings can control the local pH (*via* Donnan equilibrium) to improve the selectivity for target products during the electrochemical CO_2RR.[136] Under ideal conditions, the ionomer is thought to form a thin layer wrapping the catalyst surface. However, in the actual situation, a part of the catalyst particles may not be covered by the ionomer, while another part of the catalyst particles could be wrapped with excessive ionomers, resulting from the inhomogeneous dispersion of the catalyst ink. These situations will lead to low active site utilization or high transport resistances. Thus, optimized ionomer distributions in the catalyst inks are essential to obtain good ion transport and high active site utilization.

Drop-casting, manual airbrushing, ultrasonic spray-coating, and electrodeposition are commonly applied to prepare the CL on the GDL to form GDEs. It is important to deposit these catalyst layers uniformly in order to achieve maximum catalyst utilization. Berlinguette *et al.*[151] used X-ray fluorescence (XRF) to determine the quantity of the electrocatalyst and ionomer (Nafion, cation-exchange ionomer) loadings on the CLs prepared with different technologies. Compared with drop-casting and manual airbrushing (Fig. 8c), ultrasonic spray-coating showed the best ionomer and catalyst distributions, resulting in reproducible performance in a CO_2RR flow cell. The variations in catalyst loading and ionomer content can also affect the selectivity of the CO_2RR. By changing the catalyst loading and the ionomer to catalyst ratio, Strasser *et al.*[152] explored the mass transport in the MPL and established the

selectivity zones on the GDEs (Fig. 8d). The zone adjacent to the MPL had the maximum accessibility to the CO_2 and the furthest distance from the bulk electrolyte, creating an area with high pH and CO_2 concentration, which is ideal for the production of C_{2+} products. As the distance from the MPL increased, a CO_2-deficient zone with a lower pH value was formed, which was preferred for C_1 products such as CH_4. Moreover, CO_2 concentrations might become insufficient in the outermost area, shifting catalytic selectivity towards competition by the HER. Thus, the structure of the GDE is a key parameter to tune the selectivity of the CO_2RR.

3.2 Polymer electrolyte membrane (PEM) flow cell

Inspired by the distinguished low-temperature (<150 °C) polymer electrolyte fuel cells and water electrolyzers, polymer electrolyte membrane (PEM) flow cells are established for industrial utilization of the electrochemical CO_2RR. The PEM flow cell resolves the mass transport restrictions (low solubility of CO_2 in aqueous electrolyte solutions) occurring in the traditional H-type cell by direct gaseous CO_2 supply through GDEs.[153] Besides, recycling the reactants and products from the electrodes can keep the high feasible CO_2 concentrations at the catalyst surface, maintaining a high efficiency for the CO_2RR. In a typical PEM flow cell setup, an ion-exchange membrane is sandwiched between the cathode and anode to separate the half-reactions and conduct the ions. The PEM flow cells are generally classified into two specific configurations: zero-gap membrane flow cell and hybrid flow cell (Fig. 9a and b). The fundamental distinction between the two cells lies in the existence of liquid electrolyte flow between the cathode GDE and the membrane.[154] In the zero-gap membrane flow cell, the cathode GDE and anode GDE directly contact the membrane, which results in low ohmic resistance, low cell voltage, and high energy efficiency due to a decrease in the interelectrode distance (Table 5). For example, Janáky *et al.*[155] achieved a high selectivity of CO (FE up to 90%) and low cell voltage (2.6–3.4 V) at high partial current densities of >1.0 A cm^{-2} in a zero-gap membrane flow cell, demonstrating the advantage of low ohmic resistance in zero-gap configuration. The utilization of high ion-conductivity PEM and combination with zero-gap electrolyzer cell design made it possible for such a high partial current density, indicating the possibility for industrial application. In addition, the removal of the liquid electrolyte eliminates GDE flooding and reduces the possibility of electrocatalyst deactivation by the deposition of electrolyte impurities.[156] However, there are also some shortcomings for this kind of configuration. First, the reaction environment is difficult to adjust because of the absence of a catholyte. As we discussed in the previous sections, the electrochemical CO_2RR is relatively complicated and the target products can be influenced by the external environment. Thus, the appropriate design of GDE structures and the membrane electrode assembly is essential for regulating the microenvironments, such as the application of bilayer ionomers.[136] Second, the liquid products generated at the cathode GDE are hard to bring out by the gas flow and tend to accumulate at the GDE–membrane interface, eventually causing liquid product crossover and oxidation at the anode. For example, Sinton *et al.*[157] pointed out that over 75% of the ethanol generated at the cathode GDE migrated through the membrane to the anode in a zero-gap membrane flow cell. Furthermore, the liquid products such as formic acid and ethanol may damage the structure of the ion exchange membrane and the GDE, and possibly decrease the stability of the whole system. The hybrid flow cell with catholyte flow between the GDE and the membrane is designed to control the chemical environment near the CL. Besides, the liquid products can be brought out in a timely manner by the circulated flowing electrolyte, overcoming the product crossover problems. However, GDE flooding may occur during long-term operation, thereby resulting in the failure of the hybrid flow cell. Brushett *et al.*[158] investigated the cathode flooding in the hybrid flow cell. The Ag-cathode GDE exhibited an immediate performance failure by the GDE flooding after long-term operation for 48 h at 50 mA cm^{-2}. They also rinsed partially flooded GDEs in deionized water with subsequent drying, which restored much of the peak performance which however gradually decreased after repeated use. In addition, the presence of the electrolyte chamber leads to increased cell voltage and decreased energy efficiency. Thus, it is important to choose an appropriate flow cell for practical utilization. It is suggested that the zero-gap membrane flow cell is suitable for gas products such as CO and C_2H_4, while the hybrid flow cell is better for liquid products.[153]

The type of PEM is another important parameter for the PEM flow cell. Ion exchange membranes, which can be divided into cation exchange membranes (CEMs), anion exchange membranes (AEMs), and bipolar membranes (BPMs), have been widely applied in the PEM flow cell (Fig. 9c).[160] The ion transport pathway and pH conditions around the catalysts can be modulated using different membranes. In a CEM-based zero-gap membrane flow cell, the proton or other cations migrate from the anode to the cathode during the reaction. The accumulation of protons at the cathode side can lower the pH near the catalyst surface, providing an ideal environment for the competing hydrogen evolution reaction.[161] The migration of metal cations from the anode to the cathode leads to a gradient of metal cations between the two electrodes, increasing cell resistance and cell voltage.[148] Besides, the acidic anolyte or water coupled CEM flow cell requires precious metals (such as iridium) as oxygen evolution reaction catalysts, thus increasing the costs of the flow cell assembly. In a CEM-based hybrid flow cell, a buffer layer such as $KHCO_3$ solution between the cathode GDE and CEM can prevent an excessive amount of protons from reaching the GDE, efficiently improving the selectivity of the CO_2RR. In an AEM flow cell, OH^- or other anions like CO_3^{2-} and HCO_3^- transport through the membrane from the cathode to the anode. The water from the humidified gas stream or the membrane dissociates to provide protons for the electrochemical CO_2RR. The increased cathode pH inhibits the hydrogen evolution reaction and favors the formation of CO_2RR products.[162] Furthermore, non-precious metals are suitable for oxygen evolution reactions in alkaline environments, resulting in lower costs. However, the fed CO_2 tends to react with OH^- to

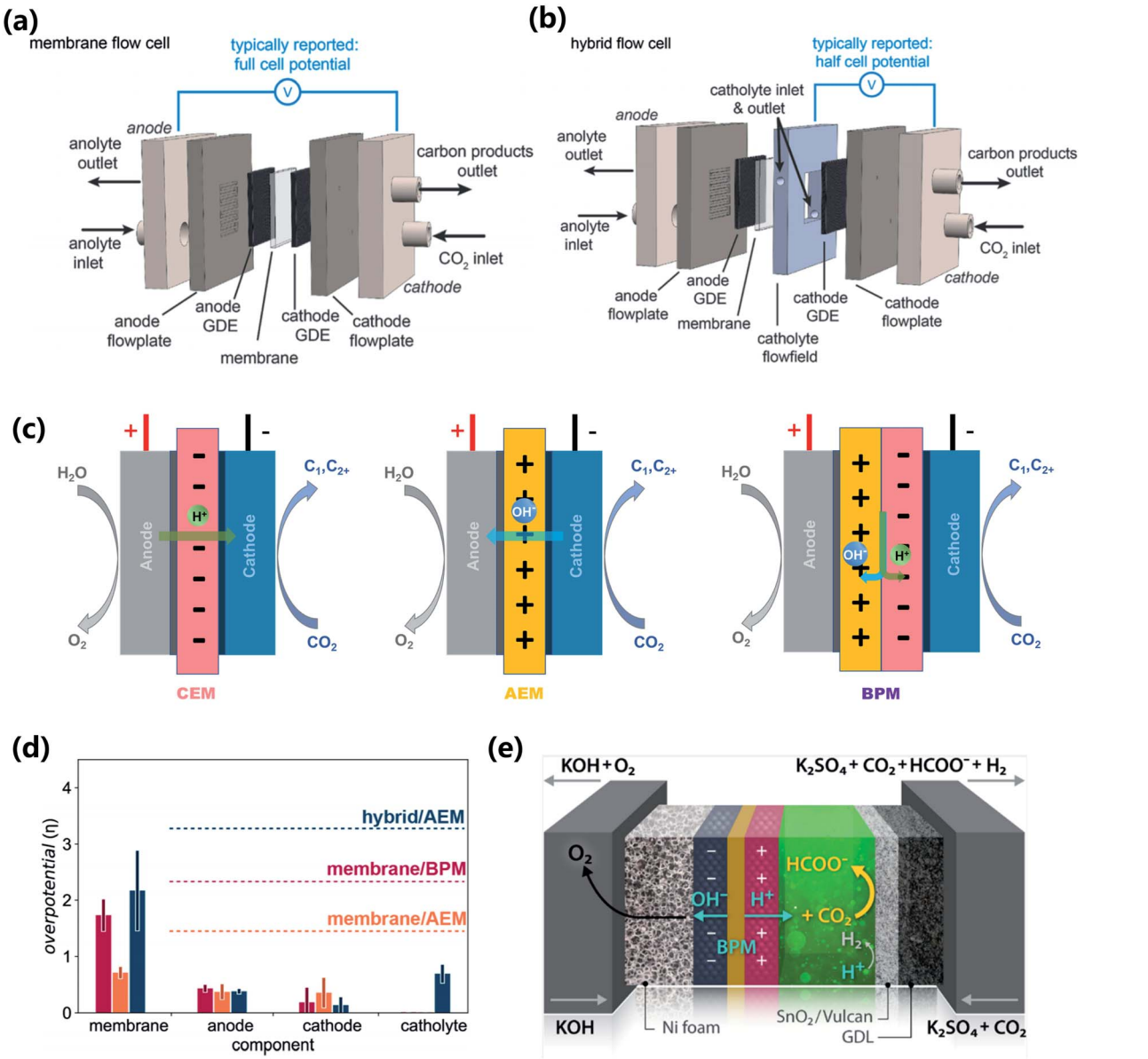

Fig. 9 (a and b) Schematic illustrations of the zero-gap membrane flow cell and hybrid flow cell. Adapted with permission.[154] Copyright 2019, American Chemical Society. (c) Schematic illustrations of electrolytic flow cells with an AEM, CEM and BPM. (d) Overpotentials at 200 mA cm^{-2} for each of the functional components in membrane/BPM (red), membrane/AEM (orange), and hybrid/AEM (navy). Adapted with permission.[154] Copyright 2019, American Chemical Society. (e) Schematic illustration of a novel cell with a thin layer of catholyte buffer. Adapted with permission.[159] Copyright 2020, American Chemical Society.

form HCO_3^- and CO_3^{2-} ions, decreasing the utilization efficiency of CO_2. Also, the HCO^{3-} and CO_3^{2-} ions can further combine with the alkali cations and generate a salt precipitate in the CO_2 gas channel, leading to lower stability of the flow cell system.[163,164] Actually, it has been shown that cation crossover from the anode to the cathode can improve the electroreduction performance, but the formation of a precipitate makes the flow cell unstable during long-term operation.[165–168] To overcome this contradiction, Janáky *et al.*[169] proposed an *operando* activation and regeneration process, where the cathode of a membrane zero-gap flow cell was periodically infused with alkali cation-containing solutions with good wetting properties. The activation was repeatable and the flow cell obtained a high performance with a CO partial current density of nearly 420 mA cm^{-2} for over 200 h.

Besides the monopolar membrane flow cell system, BPM has also been used in flow cells for electroreduction of CO_2. BPM, a special ion exchange membrane comprising a CEM and an AEM, can dissociate water into H^+ and OH^- under a reverse bias potential at the interface of CEM/AEM.[170] In a BPM flow cell system, BPM separates the catholyte and the anolyte and prevents the formation of pH gradients. The generated H^+ and OH^- ions permeate into the cathode and anode through the CEM and AEM, respectively. The produced OH^- can provide ideal alkaline conditions for the oxygen evolution reaction and a non-precious metal can be applied to decrease the cost,

Table 5 Advantages, drawbacks and characteristics of different electrolyzers for the CO_2RR

Electrolyzer type	Characteristics	Advantages	Drawbacks
Zero-gap membrane flow cell	Membrane electrode assembly	Low ohmic resistance; low cell voltage	Difficulties in reaction environment adjustment; accumulation of liquid products
Hybrid flow cell	Catholyte	Controllability of the reaction environment	GDE flooding; high solution ohmic resistance
Microfluidic flow cell	Flow channel	Adjustment of electrolyte properties; anode water management	High solution ohmic resistance; pressure sensitivity
Solid-state electrolyte (SSE) flow cell	Solid-state electrolyte	High-purity and high-concentration liquid products	High solution ohmic resistance; GDE flooding
Solid-oxide electrolysis cell (SOEC)	High temperature; solid electrolyte	Efficient mass transport; high efficiency	Extreme conditions; cell degradation

meanwhile the produced proton can be utilized in the CO_2RR. However, a large potential is required to dissociate water under reverse bias.[160] Despite some efforts that have been made to reduce the transmembrane voltage, such as interface refining[171,172] and catalyst incorporation,[173–175] there still is a high cell voltage compared with the monopolar membrane flow cell system. Berlinguette *et al.*[154] explored the excess voltages required for each flow cell component in the AEM zero-gap flow cell, BPM zero-gap flow cell, and AEM hybrid flow cell (Fig. 9d). The results indicated that the hybrid flow cell configuration suffered significant voltage loss from the catholyte and the membrane. The membrane zero-gap flow cell was more efficient than the hybrid flow cell configuration, showing lower cell voltage. The BPM zero-gap flow cell showed a higher voltage than the AEM one.[154] Another issue for the BPM zero-gap flow cell is the excess H^+ flux generated from the BPM, leading to acidic conditions at the cathode and poor CO_2RR selectivity. To settle this problem, Burdyny *et al.*[176] took advantage of the ion cross-over in BPMs to increase K^+ ion concentrations at the cathode *via* concentration diffusion. The results showed that the FE_{CO} improved from less than 20% to 68% when the anolyte $KHCO_3$ concentrations changed from 0.2 M to 3 M, a nearly 3-fold improvement as a result of increased anolyte concentrations. Another method is to insert a catholyte between the anode GDE and membrane to form a hybrid BPM flow cell. Neyerlin *et al.*[159] demonstrated that using a thin catholyte channel between the bipolar membrane and cathode GDE (Fig. 9e) enabled a robust, scalable platform for the industrial-scale device (25 cm^2 GDE), achieving a 90% FE for the CO_2RR conversion to HCOOH at 500 mA cm^{-2}. More recently, Mallouk *et al.* reported a bipolar membrane with a weak-acid cation exchange layer to suppress the competing hydrogen evolution reaction. The layer-by-layer fabricated poly(acrylic acid) (PAA)/poly(allylamine hydrochloride) (PAH) bilayer on the cation exchange layer of the BPM surface increased the local pH and served as a weak-acid cation exchanger, improving the efficiency of CO_2 electrolysis.[177]

3.3 Microfluidic flow cell

The microfluidic flow cell is one kind of membrane-free electrolytic cell. In this configuration, a liquid electrolyte is circulated through a very narrow channel (usually <1 mm thickness) to separate the cathode and anode GDEs (Fig. 10a). Kenis *et al.*[178,179] firstly reported the microfluidic reactor for CO_2-to-formate conversion using different catalysts at different pHs. High FE_{HCOOH} of 89% and energy efficiency of 45% were achieved by using a Sn catalyst at the cathode GDE.[178] They also pointed out that the flowing liquid electrolyte applied in this configuration provided many advantages: (1) this configuration enabled the adjustment of electrolyte properties (such as pH and flow rate) for ideal electrochemical CO_2RR environments; (2) the electrolyte supplied water molecules to the anode and

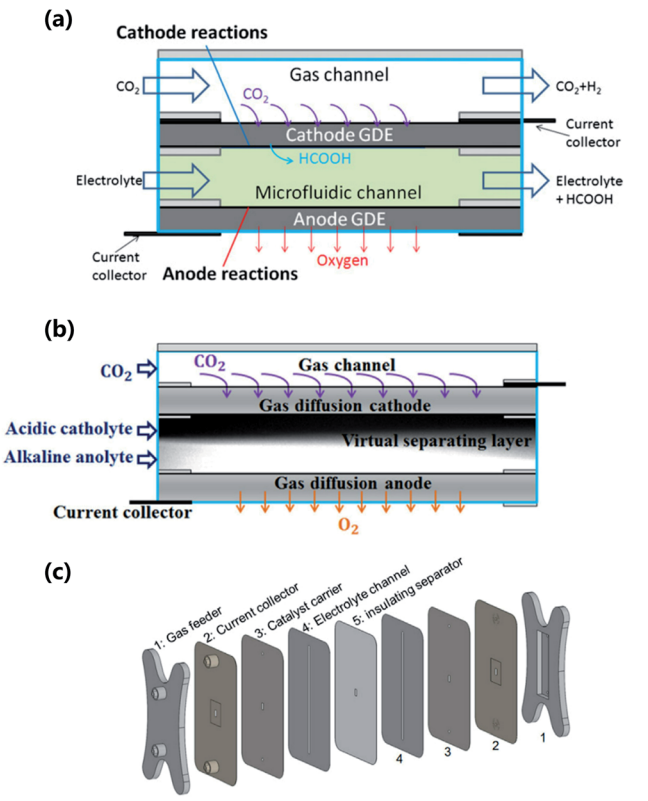

Fig. 10 (a) Schematic diagram of a microfluidic flow cell. Adapted with permission.[183] Copyright 2012, Elsevier. (b) Schematic diagram of a dual electrolyte microfluidic flow cell. (c) Component configuration of a dual electrolyte microfluidic flow cell. Adapted with permission.[180] Copyright 2016, Elsevier.

improved water management, such as avoiding anode drying; (3) the continuous flowing electrolyte could easily bring the liquid products off the cells. Xuan *et al.*[180,181] reported a dual electrolyte microfluidic flow cell for CO_2-to-HCOOH conversion, as shown in Fig. 10b and c. In a dual electrolyte system, this configuration allowed the cathode to be in a relatively acidic environment and anode in an alkaline medium, which would be respectively favorable for the electrochemical CO_2RR and oxygen evolution reaction, leading to a lower cell voltage. A peak FE_{HCOOH} of 95.6% was obtained in a pH 2 catholyte and pH 14 anolyte, which was superior to the single neutral electrolyte with an FE of 81.6%.[180] A series of analyses were also carried out to optimize the performance of dual-electrolyte microfluidic flow cells.[182–184] The results showed that the catalyst to ionomer (Nafion) ratio, microchannel thickness, electrolyte flow rate, and CO_2 supply rate were important parameters and could influence the cell performance.[182] For example, increasing the electrolyte flow rate or reducing the electrolyte channel length could increase the current density because of the decreased boundary layer thickness.[183] However, the low residence time enabled inadequate time for the reactant to move and react at the electrode surface, reducing reactant utilization.[183] More recently, Sinton *et al.*[185] combined the microfluidic flow cell and slim electrolyte flow fields in higher pressure operation with alkaline conditions to achieve a high product selectivity of the CO_2RR. The combination enabled an energy efficiency of 67% at 202 mA cm^{-2} for CO_2-to-CO conversion with a minimal electrode spacing of 0.25 mm, high pressure of 50 bar, and alkaline electrolyte of 5 M KOH.[185]

3.4 Solid-state electrolyte (SSE) flow cell

Aqueous electrolytes are usually used for the collection of the generated liquid products from the flowing cathode and for the transportation of ions between the electrodes. Consequently, the liquid fuels are contaminated with impurity ions, impeding them from being utilized directly. To separate the liquid fuels, further purification techniques must be installed. This will raise the overall cost of CO_2 conversion and hinder its decentralized generation.

In recent years, three-compartment flow cells using an SSE in the central compartment were developed to produce high-purity and high-concentration liquid products *via* the electrochemical CO_2RR. In this configuration (Fig. 11a), an AEM and a CEM are in intimate contact with the cathode and anode GDE, respectively. In the cathode compartment, a CO_2 stream is provided for the CO_2RR, while acidic solutions or a hydrogen stream is supplied in the anode compartment. An SSE layer is inserted between the AEM and CEM in the middle chamber to assist ion migration, and liquid products can be brought out of the cell by flowing water or a gas stream. Masel *et al.*[186] first applied this cell design to produce pure HCOOH solution with proton-

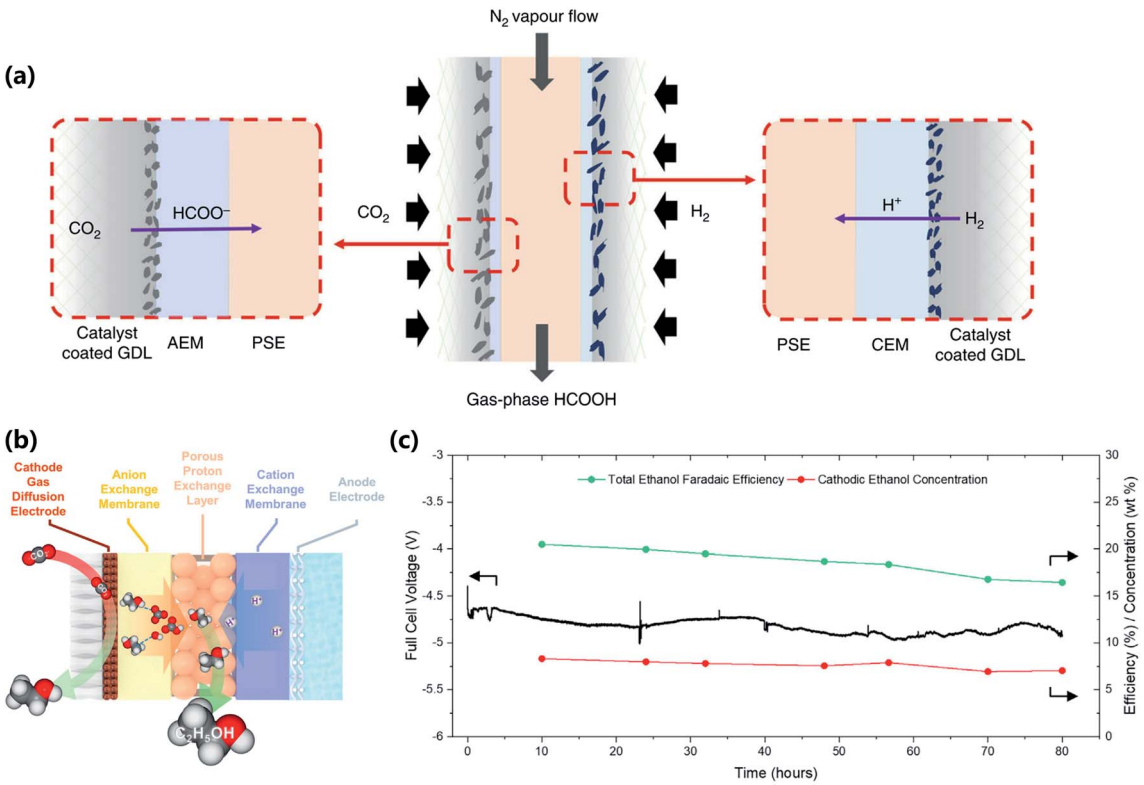

Fig. 11 (a) Schematic illustration of the CO_2 reduction cell with solid electrolyte. Adapted with permission.[188] Copyright 2020, Springer Nature. (b) Schematic illustration of the electrolyzer with the porous layer for ethanol production. (c) Voltage and product stability for a prolonged experiment run at 200 mA cm^{-2} with a 0.05 mL min^{-1} DI water flow rate through the porous layer and 0.01 M H_2SO_4 as the anolyte. Adapted with permission.[157] Copyright 2021, Elsevier.

exchanging resin as the SSE in the central compartment. The $HCOO^-$, generated at the Sn-based cathodic GDE, migrated through the AEM into the SSE compartment and combined with the proton transferred from the anodic GDE through the CEM, eventually forming the pure HCOOH and being carried out by the deionized water stream. The SSE flow cell design did not demand any aqueous salt electrolytes. Only deionized water was required for both the central SSE and the anolyte chambers, thus forming pure HCOOH solution without further separation process. The SSE flow cell could reach FE_{HCOOH} up to 94% at 140 mA cm^{-2} current density with a small full-cell voltage of 3.5 V and high stability for 550 h. More recently, they reported enhanced performance of this three-compartment design, achieving long-term stability of 1000 h at 200 mA cm^{-2} current density, providing a possible route for the commercialization of the electrochemical CO_2RR to HCOOH.[187] To improve the concentrations of the HCOOH solution, Wang *et al.*[188,189] employed a humidified or dry N_2 flow stream (Fig. 11a) as the carrier to transport the HCOOH vapors out of the porous SSE layer. High concentrations of pure HCOOH solutions (up to nearly 100 wt%) could be reached by using a suitable flow rate of the gas stream.[188] The versatility of this configuration was also demonstrated by the incorporation of various solid electrolytes into the system, such as ion-conducting polymers with $-SO_3^{2-}$ or $-NH_4^+$ functional groups and inorganic solid proton conductor $Cs_xH_{3-x}PW_{12}O_{40}$, highlighting the huge potential for industrial utilization.[189]

Anionic products are negatively charged, which can be driven by an electric field to move across the AEM into the solid-electrolyte layer. However, alcohols are neutral molecules and can only be driven across the AEM by a concentration gradient. Sinton *et al.*[157] presented the application of the SSE flow cell to block ethanol crossover to the anode (Fig. 11b) and produced concentrated ethanol at the industrial fermentation level. The porous central SSE chamber allowed the straight ethanol accumulation to raise ethanol concentrations before ethanol migrated to the anode and oxidized, thus preventing ethanol loss (less than 1%) and realizing the electrosynthesis of concentrated ethanol. The SSE flow cell continuously generated concentrated ethanol of 7.5 wt% at 200 mA cm^{-2} for over 80 h (Fig. 11c), and a maximum 13.1 wt% ethanol stream at 40 °C with an N_2 flow rate of 25 sccm through the porous SSE layer.

The introduction of an SSE into the CO_2RR electrolyzer provides a new pathway to generate high-purity and high-concentration liquid products. However, the poor stability of the SSE and ion-exchange membranes during long-term operation is still a daunting challenge. Specifically, the organic products will damage the structure of the SSE and ion-exchange membranes, eventually degrading the performance of the SSE flow cell.[190,191] Moreover, high concentration organics will facilitate the crossover of the products, causing them to be oxidized at the anode and degrading the conversion efficiencies.[191]

3.5 Solid-oxide electrolysis cell (SOEC)

Besides low-temperature flow cell configurations, high-temperature (>600 °C) solid oxide electrolysis cells (SOECs) have also been explored for CO_2 electrolysis.[192] In comparison to the electrochemical CO_2RR at low temperatures, high operating temperatures can increase the activity of the catalysts and reduce the ohmic resistance, resulting in high current density and low cell voltage. Besides, the high-temperature electrochemical CO_2RR coupled with industrial waste heat and renewable energy can lower the operation cost for CO_2 electrolysis. In a typical SOEC configuration, a solid electrolyte is sandwiched between the well-refined anode and cathode to transport ions. SOECs can be classified into two types based on the solid electrolyte: oxygen ion-conducting electrolyte (O-SOEC) and proton-conducting electrolyte (H-SOEC) (Fig. 12a and b). In O-SOECs, gaseous CO_2 can directly diffuse into the porous cathode and then be reduced to CO. The oxygen ions, produced at the cathode during the electroreduction, migrate to the anode through the solid electrolyte and are oxidized to produce oxygen. Meanwhile, in H-SOECs, the protons generated from the oxidation of H_2O at the anode will be transferred to the cathode and then react with CO_2 to produce CO and other chemicals. Thus, it can be seen that the solid electrolyte should have high ion conductivity and excellent gas tightness to separate the produced CO and O_2. So far, the electrolytes for O-SOEC mainly include stabilized zirconia and doped lanthanum

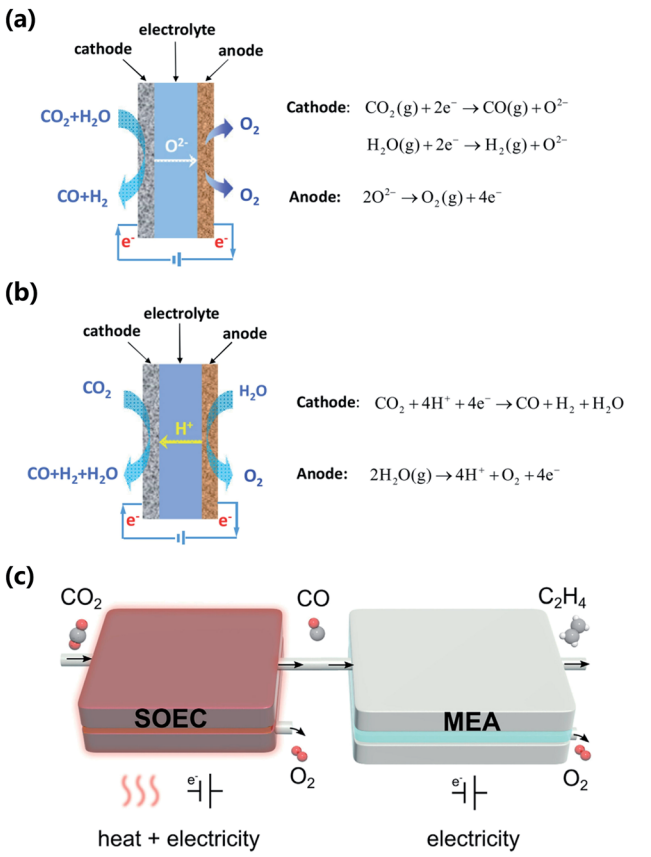

Fig. 12 (a) SOEC schematics and the reaction paths in O-SOEC. (b) SOEC schematics and the reaction paths in H-SOEC. Adapted with permission.[192] Copyright 2017, Elsevier BV. (c) Schematic illustration of the SOEC–MEA cascade approach for CO_2-to-C_2H_4 conversion. Adapted with permission.[194] Copyright 2021, Elsevier.

gallium, while electrolytes for H-SOEC are usually perovskite-structured oxides, zirconates, and alkaline earth cerates.[193]

Generally, the main product of SOECs is CO; the high thermal efficiency and reliability of the system achieve an efficient CO generation. However, generation of other C_1 and C_{2+} products is limited, because the intermediate species are quickly desorbed off the electrode surface at high temperatures.[19] Sinton *et al.*[194] proposed a cascade approach to use an SOEC and membrane electrode assembly (MEA) flow cell for CO_2-to-C_2H_4 conversion (Fig. 12c). In the SOEC–MEA cascade system, CO_2 was firstly electroreduced to CO in the SOEC. Then the CO was used as the feed gas in the MEA flow cell for further reduction to C_2H_4. This SOEC–MEA cascade system integrated the advantage of high efficiency for CO_2-to-CO conversion of the SOEC and the elimination of CO_2 loss to carbonate in the MEA flow cell, improving the CO_2 utilization efficiency. In spite of the high efficiency of SOECs, cell degradation is the key drawback for the industrial utilization of SOECs. More efforts need to be made to improve the stability of SOEC systems.

4. Conclusion and outlook

The electrochemical CO_2RR provides an attractive pathway for the conversion of CO_2 into value-added chemicals and fuels as carriers for the transport and storage of renewable energy. In this review, we present representative electrocatalysts for refining the selectivity of different products, such as metal-free catalysts and metal nanoparticles, and industrial-scale electrolyzers including low-temperature flow cells and high-temperature SOECs. The selectivity and catalytic performance of catalysts are not only related to their inherent properties, but also depend on their structures and morphologies. Optimization of electrocatalysts is essential for highly efficient CO_2 conversion. In addition, electrolyzer configuration engineering is a pivotal technique for industrial-scale CO_2 electrolysis. With the utilization of GDEs, vapor-fed CO_2 electrolyzers hold promise for commercializing the electrochemical CO_2RR to value-added chemicals and fuels. PEM flow cells are the most commonly used reactors because of their low cell resistance and high mass transport. Microfluidic flow cells possess the advantages of adjustable pH environments and well-refined anode water management. The implementation of an SSE in a three-compartment flow cell enables the generation of high-purity and high-concentration liquid products without further separation process. High-temperature SOECs can highly activate the electrocatalysts, making the reduction process more efficient.

Despite the significant advances that have been achieved in the last few decades, the performance of the CO_2RR is still far from industrial application. In addition to the catalyst development as outlined in Section 2, other aspects are challenging as follows: (1) understanding the reaction mechanisms of the CO_2RR for different catalysts is essential for electrocatalyst design and optimization. *In situ* and *operando* spectroscopic techniques such as Raman and synchrotron X-ray diffraction should be applied to explore the mechanism. (2) The criteria of electrochemical cells should be established, such as the electrolyte types, flow rates, and operating conditions, so that the comparison of literature data is convincing and practical. (3) Methods for preparing a catalyst layer in the flow cells should be refined for maximum utilization and high efficiency. Most catalyst layers on the GDE are prepared by drop-casting and manual airbrushing, which usually leads to aggregation issues. The recent ultrasonic spray-coating technique achieves uniform catalyst layers, but the high cost of equipment makes industrial utilization difficult. Developing new catalyst layer preparation methods can further improve the efficiency of the whole cell. (4) Optimizing ion exchange membranes is needed to minimize product crossover and improve mechanical and chemical stability. The membrane is the pivotal component for the most commonly used PEM flow cell. Refining the membranes can improve the stability and efficiency of the CO_2RR. (5) CO_2 utilization efficiency should be further highlighted. Most reports focus on the FE of CO_2 conversion for active catalysts, while strategies to improve CO_2 utilization efficiency are often less reported.

The electrochemical reduction of CO_2 to value-added chemicals is critical for achieving a neutral carbon cycle to mitigate the energy and environmental crisis. Although there are still some challenging issues, a better understanding of the reaction mechanism, well-designed catalysts, and optimized electrolyzers, together with advances in other technologies such as solar cells and CO_2 capture, will further reduce the cost and make the CO_2RR practical for industrial applications.

Author contributions

Geng Li: data curation and writing – original draft; Yong Liu: data curation; Qiang Zhang: data curation; Qiushi Hu: data curation; Weihua Guo: data curation; Xiaohu Cao: data curation; Yubing Dou: data curation; Le Cheng: data curation; Yun Song: data curation; Jianjun Su: data curation; Libei Huang: data curation; Ruquan Ye: supervision, funding acquisition and writing – review & editing.

Conflicts of interest

There are no conflicts of interest to declare.

Acknowledgements

R. Y. acknowledges the support from the Guangdong Basic and Applied Basic Research Fund (No. 2022A1515011333), the Science, Technology and Innovation Commission of Shenzhen under Shenzhen Virtual University Park Special Fund (No. 2021Szvup129), and the Hong Kong Research Grant Council under Early Career Scheme (No. 21300620).

Notes and references

1 D. W. Keith, *Science*, 2009, **325**, 1654–1655.
2 C. S. Galik, *Nat. Clim. Change*, 2019, **10**, 2–3.
3 C. Wang, K. Jiang, T. W. Jones, S. Yang, H. Yu, P. Feron and K. Li, *Chem. Eng. J.*, 2022, **427**, 131981.

4 G. D. Patrón and L. Ricardez-Sandoval, *Appl. Energy*, 2022, **308**, 118302.
5 M. Van der Spek, T. Fout, M. Garcia, V. N. Kuncheekanna, M. Matuszewski, S. McCoy, J. Morgan, S. M. Nazir, A. Ramirez and S. Roussanaly, *Int. J. Greenhouse Gas Control*, 2020, **100**, 103113.
6 T. Zhang, W. Zhang, R. Yang, Y. Liu and M. Jafari, *J. Cleaner Prod.*, 2021, **281**, 124409.
7 D. Zhu, S. Peng, S. Zhao, M. Wei and B. Bai, *Energy Fuels*, 2021, **35**, 4711–4742.
8 A. Bogaerts and G. Centi, *Front. Energy. Res.*, 2020, **8**, 111–118.
9 A. Saravanan, D.-V. N. Vo, S. Jeevanantham, V. Bhuvaneswari, V. A. Narayanan, P. Yaashikaa, S. Swetha and B. Reshma, *Chem. Eng. Sci.*, 2021, **236**, 116515.
10 I. Sullivan, A. Goryachev, I. A. Digdaya, X. Li, H. A. Atwater, D. A. Vermaas and C. Xiang, *Nat. Catal.*, 2021, **4**, 952–958.
11 S. Jin, Z. Hao, K. Zhang, Z. Yan and J. Chen, *Angew. Chem., Int. Ed.*, 2021, **60**, 20627–20648.
12 S. Zhu, E. P. Delmo, T. Li, X. Qin, J. Tian, L. Zhang and M. Shao, *Adv. Mater.*, 2021, **33**, 2005484.
13 Y. Zheng, Y. Wang, Y. Yuan and H. Huang, *ChemNanoMat*, 2021, **7**, 502–514.
14 K. Chan, *Nat. Commun.*, 2020, **11**, 5954–5958.
15 L. Sun, V. Reddu, A. C. Fisher and X. Wang, *Energy Environ. Sci.*, 2020, **13**, 374–403.
16 L. Fan, C. Xia, F. Yang, J. Wang, H. Wang and Y. Lu, *Sci. Adv.*, 2020, **6**, eaay3111.
17 H. Ju, G. Kaur, A. P. Kulkarni and S. Giddey, *J. CO2 Util.*, 2019, **32**, 178–186.
18 R. I. Masel, Z. Liu, H. Yang, J. J. Kaczur, D. Carrillo, S. Ren, D. Salvatore and C. P. Berlinguette, *Nat. Nanotechnol.*, 2021, **16**, 118–128.
19 S. Liang, N. Altaf, L. Huang, Y. Gao and Q. Wang, *J. CO2 Util.*, 2020, **35**, 90–105.
20 F.-Y. Gao, R.-C. Bao, M.-R. Gao and S.-H. Yu, *J. Mater. Chem. A*, 2020, **8**, 15458–15478.
21 Y. Xue, Y. Guo, H. Cui and Z. Zhou, *Small Methods*, 2021, **5**, e2100736.
22 Q. Wang, C. Cai, M. Dai, J. Fu, X. Zhang, H. Li, H. Zhang, K. Chen, Y. Lin, H. Li, J. Hu, M. Miyauchi and M. Liu, *Small Sci.*, 2020, **1**, 156–162.
23 S. Chatterjee, C. Griego, J. L. Hart, Y. Li, M. L. Taheri, J. Keith and J. D. Snyder, *ACS Catal.*, 2019, **9**, 5290–5301.
24 S. Popovic, M. Smiljanic, P. Jovanovic, J. Vavra, R. Buonsanti and N. Hodnik, *Angew. Chem., Int. Ed.*, 2020, **59**, 14736–14746.
25 W. Yuan, Y. Ma, H. Wu and L. Cheng, *J. Energy Chem.*, 2022, **65**, 254–279.
26 R. Francke, B. Schille and M. Roemelt, *Chem. Rev.*, 2018, **118**, 4631–4701.
27 S. A. Mahyoub, F. A. Qaraah, C. Chen, F. Zhang, S. Yan and Z. Cheng, *Sustainable Energy Fuels*, 2020, **4**, 50–67.
28 C. Kim, H. S. Jeon, T. Eom, M. S. Jee, H. Kim, C. M. Friend, B. K. Min and Y. J. Hwang, *J. Am. Chem. Soc.*, 2015, **137**, 13844–13850.
29 S. Liu, H. Tao, L. Zeng, Q. Liu, Z. Xu, Q. Liu and J. L. Luo, *J. Am. Chem. Soc.*, 2017, **139**, 2160–2163.
30 K. Qi, Y. Zhang, J. Li, C. Charmette, M. Ramonda, X. Cui, Y. Wang, Y. Zhang, H. Wu, W. Wang, X. Zhang and D. Voiry, *ACS Nano*, 2021, **15**, 7682–7693.
31 S. C. Abeyweera, J. Yu, J. P. Perdew, Q. Yan and Y. Sun, *Nano Lett.*, 2020, **20**, 2806–2811.
32 D. Sun, X. Xu, Y. Qin, S. P. Jiang and Z. Shao, *ChemSusChem*, 2020, **13**, 39–58.
33 X. Peng, S. G. Karakalos and W. E. Mustain, *ACS Appl. Mater. Interfaces*, 2018, **10**, 1734–1742.
34 J. Rosen, G. S. Hutchings, Q. Lu, S. Rivera, Y. Zhou, D. G. Vlachos and F. Jiao, *ACS Catal.*, 2015, **5**, 4293–4299.
35 S. Zhang, Q. Fan, R. Xia and T. J. Meyer, *Acc. Chem. Res.*, 2020, **53**, 255–264.
36 S. Ren, D. Joulie, D. Salvatore, K. Torbensen, M. Wang, M. Robert and C. P. Berlinguette, *Science*, 2019, **365**, 367–369.
37 X. Wu, J. W. Sun, P. F. Liu, J. Y. Zhao, Y. Liu, L. Guo, S. Dai, H. G. Yang and H. Zhao, *Adv. Funct. Mater.*, 2022, **32**, 2107301.
38 M. Wang, K. Torbensen, D. Salvatore, S. Ren, D. Joulie, F. Dumoulin, D. Mendoza, B. Lassalle-Kaiser, U. Isci, C. P. Berlinguette and M. Robert, *Nat. Commun.*, 2019, **10**, 3602–3610.
39 M. Zhu, R. Ye, K. Jin, N. Lazouski and K. Manthiram, *ACS Energy Lett.*, 2018, **3**, 1381–1386.
40 R. Ye, Y. Chyan, J. Zhang, Y. Li, X. Han, C. Kittrell and J. M. Tour, *Adv. Mater.*, 2017, **29**, 1702211.
41 L. Huang, S. Xu, Z. Wang, K. Xue, J. Su, Y. Song, S. Chen, C. Zhu, B. Z. Tang and R. Ye, *ACS Nano*, 2020, **14**, 12045–12053.
42 S. He, Y. Hong, M. Liao, Y. Li, L. Qiu and H. Peng, *Aggregate*, 2021, **2**, e143.
43 M. Zhu, J. Chen, L. Huang, R. Ye, J. Xu and Y. F. Han, *Angew. Chem., Int. Ed.*, 2019, **58**, 6595–6599.
44 Y. Wu, Y. Liang and H. Wang, *Acc. Chem. Res.*, 2021, **54**, 3148–3159.
45 J. Su, J.-J. Zhang, J. Chen, Y. Song, L. Huang, M. Zhu, B. I. Yakobson, B. Z. Tang and R. Ye, *Energy Environ. Sci.*, 2021, **14**, 483–492.
46 Y. Yue, P. Cai, K. Xu, H. Li, H. Chen, H. C. Zhou and N. Huang, *J. Am. Chem. Soc.*, 2021, **143**, 18052–18060.
47 Y. Song, J.-J. Zhang, Z. Zhu, X. Chen, L. Huang, J. Su, Z. Xu, T. H. Ly, C.-S. Lee and B. I. Yakobson, *Appl. Catal., B*, 2021, **284**, 119750.
48 L. Jiao, W. Yang, G. Wan, R. Zhang, X. Zheng, H. Zhou, S. H. Yu and H. L. Jiang, *Angew. Chem., Int. Ed.*, 2020, **59**, 20589–20595.
49 W. Zheng, F. Chen, Q. Zeng, Z. Li, B. Yang, L. Lei, Q. Zhang, F. He, X. Wu and Y. Hou, *Nano-Micro Lett.*, 2020, **12**, 108–120.
50 Y. Guo, S. Yao, Y. Xue, X. Hu, H. Cui and Z. Zhou, *Appl. Catal., B*, 2022, **304**, 120997.
51 H. Zhang, J. Li, S. Xi, Y. Du, X. Hai, J. Wang, H. Xu, G. Wu, J. Zhang, J. Lu and J. Wang, *Angew. Chem., Int. Ed.*, 2019, **58**, 14871–14876.

52 N. Leonard, W. Ju, I. Sinev, J. Steinberg, F. Luo, A. S. Varela, B. Roldan Cuenya and P. Strasser, *Chem. Sci.*, 2018, **9**, 5064–5073.
53 X.-M. Hu, H. H. Hval, E. T. Bjerglund, K. J. Dalgaard, M. R. Madsen, M.-M. Pohl, E. Welter, P. Lamagni, K. B. Buhl, M. Bremholm, M. Beller, S. U. Pedersen, T. Skrydstrup and K. Daasbjerg, *ACS Catal.*, 2018, **8**, 6255–6264.
54 F. Yang, P. Song, X. Liu, B. Mei, W. Xing, Z. Jiang, L. Gu and W. Xu, *Angew. Chem., Int. Ed.*, 2018, **57**, 12303–12307.
55 P. Hou, W. Song, X. Wang, Z. Hu and P. Kang, *Small*, 2020, **16**, e2001896.
56 X. Wang, Z. Chen, X. Zhao, T. Yao, W. Chen, R. You, C. Zhao, G. Wu, J. Wang, W. Huang, J. Yang, X. Hong, S. Wei, Y. Wu and Y. Li, *Angew. Chem., Int. Ed.*, 2018, **57**, 1944–1948.
57 Z. Geng, Y. Cao, W. Chen, X. Kong, Y. Liu, T. Yao and Y. Lin, *Appl. Catal., B*, 2019, **240**, 234–240.
58 W. Zhu, L. Zhang, S. Liu, A. Li, X. Yuan, C. Hu, G. Zhang, W. Deng, K. Zang, J. Luo, Y. Zhu, M. Gu, Z. J. Zhao and J. Gong, *Angew. Chem., Int. Ed.*, 2020, **59**, 12664–12668.
59 D. Mellmann, P. Sponholz, H. Junge and M. Beller, *Chem. Soc. Rev.*, 2016, **45**, 3954–3988.
60 J. T. Feaster, C. Shi, E. R. Cave, T. Hatsukade, D. N. Abram, K. P. Kuhl, C. Hahn, J. K. Nørskov and T. F. Jaramillo, *ACS Catal.*, 2017, **7**, 4822–4827.
61 X. An, S. Li, A. Yoshida, Z. Wang, X. Hao, A. Abudula and G. Guan, *ACS Sustainable Chem. Eng.*, 2019, **7**, 9360–9368.
62 S. Ning, J. Wang, D. Xiang, S. Huang, W. Chen, S. Chen and X. Kang, *J. Catal.*, 2021, **399**, 67–74.
63 J. Wu, X. Bai, Z. Ren, S. Du, Z. Song, L. Zhao, B. Liu, G. Wang and H. Fu, *Nano Res.*, 2020, **14**, 1053–1060.
64 S. Liu, J. Xiao, X. F. Lu, J. Wang, X. Wang and X. W. D. Lou, *Angew. Chem., Int. Ed.*, 2019, **58**, 8499–8503.
65 Z. Chen, T. Fan, Y.-Q. Zhang, J. Xiao, M. Gao, N. Duan, J. Zhang, J. Li, Q. Liu, X. Yi and J.-L. Luo, *Appl. Catal., B*, 2020, **261**, 118243.
66 Y. Cheng, J. Hou and P. Kang, *ACS Energy Lett.*, 2021, **6**, 3352–3358.
67 Y. X. Duan, K. H. Liu, Q. Zhang, J. M. Yan and Q. Jiang, *Small Methods*, 2020, **4**, 1900846.
68 J. Yang, X. Wang, Y. Qu, X. Wang, H. Huo, Q. Fan, J. Wang, L. M. Yang and Y. Wu, *Adv. Energy Mater.*, 2020, **10**, 2001709.
69 K. Fan, Y. Jia, Y. Ji, P. Kuang, B. Zhu, X. Liu and J. Yu, *ACS Catal.*, 2019, **10**, 358–364.
70 S. Q. Liu, E. Shahini, M. R. Gao, L. Gong, P. F. Sui, T. Tang, H. Zeng and J. L. Luo, *ACS Nano*, 2021, **15**, 17757–17768.
71 S. Liu, X. F. Lu, J. Xiao, X. Wang and X. W. D. Lou, *Angew. Chem., Int. Ed.*, 2019, **58**, 13828–13833.
72 Z. Chen, K. Mou, X. Wang and L. Liu, *Angew. Chem., Int. Ed.*, 2018, **57**, 12790–12794.
73 Z. Wu, H. Wu, W. Cai, Z. Wen, B. Jia, L. Wang, W. Jin and T. Ma, *Angew. Chem., Int. Ed.*, 2021, **60**, 12554–12559.
74 X. An, S. Li, A. Yoshida, T. Yu, Z. Wang, X. Hao, A. Abudula and G. Guan, *ACS Appl. Mater. Interfaces*, 2019, **11**, 42114–42122.
75 Y. X. Duan, Y. T. Zhou, Z. Yu, D. X. Liu, Z. Wen, J. M. Yan and Q. Jiang, *Angew. Chem., Int. Ed.*, 2021, **60**, 8798–8802.
76 J. Wang, J. Zou, X. Hu, S. Ning, X. Wang, X. Kang and S. Chen, *J. Mater. Chem. A*, 2019, **7**, 27514–27521.
77 B. Wei, Y. Xiong, Z. Zhang, J. Hao, L. Li and W. Shi, *Appl. Catal., B*, 2021, **283**, 119646.
78 I. S. Kwon, T. T. Debela, I. H. Kwak, H. W. Seo, K. Park, D. Kim, S. J. Yoo, J.-G. Kim, J. Park and H. S. Kang, *J. Mater. Chem. A*, 2019, **7**, 22879–22883.
79 M. Qi, J. Park, R. S. Landon, J. Kim, Y. Liu and I. Moon, *Renewable Sustainable Energy Rev.*, 2022, **153**, 111732.
80 Y.-L. Qiu, H.-X. Zhong, T.-T. Zhang, W.-B. Xu, X.-F. Li and H.-M. Zhang, *ACS Catal.*, 2017, **7**, 6302–6310.
81 K. J. P. Schouten, E. Pérez Gallent and M. T. M. Koper, *ACS Catal.*, 2013, **3**, 1292–1295.
82 E. Perez-Gallent, G. Marcandalli, M. C. Figueiredo, F. Calle-Vallejo and M. T. M. Koper, *J. Am. Chem. Soc.*, 2017, **139**, 16412–16419.
83 G. L. De Gregorio, T. Burdyny, A. Loiudice, P. Iyengar, W. A. Smith and R. Buonsanti, *ACS Catal.*, 2020, **10**, 4854–4862.
84 P. Iyengar, J. Huang, G. L. De Gregorio, C. Gadiyar and R. Buonsanti, *Chem. Commun.*, 2019, **55**, 8796–8799.
85 Y. Li, F. Cui, M. B. Ross, D. Kim, Y. Sun and P. Yang, *Nano Lett.*, 2017, **17**, 1312–1317.
86 H. Liu, K. Xiang, Y. Liu, F. Zhu, M. Zou, X. Yan and L. Chai, *ChemElectroChem*, 2018, **5**, 3991–3999.
87 W. Zhu, L. Zhang, P. Yang, X. Chang, H. Dong, A. Li, C. Hu, Z. Huang, Z. J. Zhao and J. Gong, *Small*, 2018, **14**, 1703314.
88 R. Wang, R. Jiang, C. Dong, T. Tong, Z. Li, H. Liu and X.-W. Du, *Ind. Eng. Chem. Res.*, 2020, **60**, 273–280.
89 C. Choi, J. Cai, C. Lee, H. M. Lee, M. Xu and Y. Huang, *Nano Res.*, 2021, **14**, 3497–3501.
90 W. J. Dong, J. W. Lim, D. M. Hong, J. Kim, J. Y. Park, W. S. Cho, S. Baek and J. L. Lee, *ACS Appl. Mater. Interfaces*, 2021, **13**, 18905–18913.
91 S. Singh, R. K. Gautam, K. Malik and A. Verma, *J. CO2 Util.*, 2017, **18**, 139–146.
92 A. Guan, Z. Chen, Y. Quan, C. Peng, Z. Wang, T.-K. Sham, C. Yang, Y. Ji, L. Qian, X. Xu and G. Zheng, *ACS Energy Lett.*, 2020, **5**, 1044–1053.
93 Y. Cai, J. Fu, Y. Zhou, Y. C. Chang, Q. Min, J. J. Zhu, Y. Lin and W. Zhu, *Nat. Commun.*, 2021, **12**, 586–595.
94 S. Chen, B. Wang, J. Zhu, L. Wang, H. Ou, Z. Zhang, X. Liang, L. Zheng, L. Zhou, Y. Q. Su, D. Wang and Y. Li, *Nano Lett.*, 2021, **21**, 7325–7331.
95 W. Ju, A. Bagger, X. Wang, Y. Tsai, F. Luo, T. Möller, H. Wang, J. Rossmeisl, A. S. Varela and P. Strasser, *ACS Energy Lett.*, 2019, **4**, 1663–1671.
96 L. Han, S. Song, M. Liu, S. Yao, Z. Liang, H. Cheng, Z. Ren, W. Liu, R. Lin, G. Qi, X. Liu, Q. Wu, J. Luo and H. L. Xin, *J. Am. Chem. Soc.*, 2020, **142**, 12563–12567.
97 Y. Ouyang, L. Shi, X. Bai, Q. Li and J. Wang, *Chem. Sci.*, 2020, **11**, 1807–1813.
98 S. Wang, L. Li, J. Li, C. Yuan, Y. Kang, K. S. Hui, J. Zhang, F. Bin, X. Fan, F. Chen and K. N. Hui, *J. Phys. Chem. C*, 2021, **125**, 7155–7165.

99 Z. Chen, M.-R. Gao, Y.-Q. Zhang, N. Duan, T. Fan, J. Xiao, J. Zhang, Y. Dong, J. Li, X. Yi and J.-L. Luo, *Nano Energy*, 2020, **73**, 104833.
100 G. Qin, Q. Cui, A. Du and Q. Sun, *ChemCatChem*, 2020, **12**, 1483–1490.
101 T. Zhang, W. Li, K. Huang, H. Guo, Z. Li, Y. Fang, R. M. Yadav, V. Shanov, P. M. Ajayan, L. Wang, C. Lian and J. Wu, *Nat. Commun.*, 2021, **12**, 5265–5274.
102 M. Huang, S. Gong, C. Wang, Y. Yang, P. Jiang, P. Wang, L. Hu and Q. Chen, *Angew. Chem., Int. Ed.*, 2021, **133**, 23184–23191.
103 S.-N. Sun, J.-N. Lu, Q. Li, L.-Z. Dong, Q. Huang, J. Liu and Y.-Q. Lan, *Chem. Catal.*, 2021, **1**, 1133–1144.
104 Y. Pei, H. Zhong and F. Jin, *Energy Sci. Eng.*, 2021, **9**, 1012–1032.
105 J. Albo, M. Alvarez-Guerra, P. Castaño and A. Irabien, *Green Chem.*, 2015, **17**, 2304–2324.
106 H.-P. Yang, S. Qin, H. Wang and J.-X. Lu, *Green Chem.*, 2015, **17**, 5144–5148.
107 W. Zhang, Q. Qin, L. Dai, R. Qin, X. Zhao, X. Chen, D. Ou, J. Chen, T. T. Chuong, B. Wu and N. Zheng, *Angew. Chem., Int. Ed.*, 2018, **57**, 9475–9479.
108 M. Le, M. Ren, Z. Zhang, P. T. Sprunger, R. L. Kurtz and J. C. Flake, *J. Electrochem. Soc.*, 2011, **158**, E45.
109 M. Irfan Malik, Z. O. Malaibari, M. Atieh and B. Abussaud, *Chem. Eng. Sci.*, 2016, **152**, 468–477.
110 J. Albo, A. Sáez, J. Solla-Gullón, V. Montiel and A. Irabien, *Appl. Catal., B*, 2015, **176**, 709–717.
111 J. Albo and A. Irabien, *J. Catal.*, 2016, **343**, 232–239.
112 D. Yang, Q. Zhu, C. Chen, H. Liu, Z. Liu, Z. Zhao, X. Zhang, S. Liu and B. Han, *Nat. Commun.*, 2019, **10**, 677–686.
113 F. Jia, X. Yu and L. Zhang, *J. Power Sources*, 2014, **252**, 85–89.
114 L. Lu, X. Sun, J. Ma, D. Yang, H. Wu, B. Zhang, J. Zhang and B. Han, *Angew. Chem., Int. Ed.*, 2018, **57**, 14149–14153.
115 J. Huang, Q. Hu, X. Guo, Q. Zeng and L. Wang, *Green Chem.*, 2018, **20**, 2967–2972.
116 E. Boutin, M. Wang, J. C. Lin, M. Mesnage, D. Mendoza, B. Lassalle-Kaiser, C. Hahn, T. F. Jaramillo and M. Robert, *Angew. Chem., Int. Ed.*, 2019, **58**, 16172–16176.
117 Y. Wu, Z. Jiang, X. Lu, Y. Liang and H. Wang, *Nature*, 2019, **575**, 639–642.
118 S. Gonglach, S. Paul, M. Haas, F. Pillwein, S. S. Sreejith, S. Barman, R. De, S. Mullegger, P. Gerschel, U. P. Apfel, H. Coskun, A. Aljabour, P. Stadler, W. Schofberger and S. Roy, *Nat. Commun.*, 2019, **10**, 3864–3874.
119 R. De, S. Gonglach, S. Paul, M. Haas, S. S. Sreejith, P. Gerschel, U. P. Apfel, T. H. Vuong, J. Rabeah, S. Roy and W. Schöfberger, *Angew. Chem., Int. Ed.*, 2020, **59**, 10527–10534.
120 H. M. Jeong, Y. Kwon, J. H. Won, Y. Lum, M. J. Cheng, K. H. Kim, M. Head-Gordon and J. K. Kang, *Adv. Energy Mater.*, 2020, **10**, 2070041.
121 W. Luo, X. Nie, M. J. Janik and A. Asthagiri, *ACS Catal.*, 2015, **6**, 219–229.
122 W. Fu, Z. Liu, T. Wang, J. Liang, S. Duan, L. Xie, J. Han and Q. Li, *ACS Sustainable Chem. Eng.*, 2020, **8**, 15223–15229.
123 M. Wu, C. Zhu, K. Wang, G. Li, X. Dong, Y. Song, J. Xue, W. Chen, W. Wei and Y. Sun, *ACS Appl. Mater. Interfaces*, 2020, **12**, 11562–11569.
124 H. Huo, J. Wang, Q. Fan, Y. Hu and J. Yang, *Adv. Energy Mater.*, 2021, **11**, 2102447.
125 X. Wei, Z. Yin, K. Lyu, Z. Li, J. Gong, G. Wang, L. Xiao, J. Lu and L. Zhuang, *ACS Catal.*, 2020, **10**, 4103–4111.
126 C. W. Li and M. W. Kanan, *J. Am. Chem. Soc.*, 2012, **134**, 7231–7234.
127 H. Jung, S. Y. Lee, C. W. Lee, M. K. Cho, D. H. Won, C. Kim, H. S. Oh, B. K. Min and Y. J. Hwang, *J. Am. Chem. Soc.*, 2019, **141**, 4624–4633.
128 Q. Lei, H. Zhu, K. Song, N. Wei, L. Liu, D. Zhang, J. Yin, X. Dong, K. Yao, N. Wang, X. Li, B. Davaasuren, J. Wang and Y. Han, *J. Am. Chem. Soc.*, 2020, **142**, 4213–4222.
129 T. Kim and G. T. R. Palmore, *Nat. Commun.*, 2020, **11**, 3622–3631.
130 R. M. Arán-Ais, F. Scholten, S. Kunze, R. Rizo and B. Roldan Cuenya, *Nat. Energy*, 2020, **5**, 317–325.
131 P. De Luna, R. Quintero-Bermudez, C.-T. Dinh, M. B. Ross, O. S. Bushuyev, P. Todorović, T. Regier, S. O. Kelley, P. Yang and E. H. Sargent, *Nat. Catal.*, 2018, **1**, 103–110.
132 Z. Q. Liang, T. T. Zhuang, A. Seifitokaldani, J. Li, C. W. Huang, C. S. Tan, Y. Li, P. De Luna, C. T. Dinh, Y. Hu, Q. Xiao, P. L. Hsieh, Y. Wang, F. Li, R. Quintero-Bermudez, Y. Zhou, P. Chen, Y. Pang, S. C. Lo, L. J. Chen, H. Tan, Z. Xu, S. Zhao, D. Sinton and E. H. Sargent, *Nat. Commun.*, 2018, **9**, 3828–3837.
133 P. P. Yang, X. L. Zhang, F. Y. Gao, Y. R. Zheng, Z. Z. Niu, X. Yu, R. Liu, Z. Z. Wu, S. Qin, L. P. Chi, Y. Duan, T. Ma, X. S. Zheng, J. F. Zhu, H. J. Wang, M. R. Gao and S. H. Yu, *J. Am. Chem. Soc.*, 2020, **142**, 6400–6408.
134 M. S. Xie, B. Y. Xia, Y. Li, Y. Yan, Y. Yang, Q. Sun, S. H. Chan, A. Fisher and X. Wang, *Energy Environ. Sci.*, 2016, **9**, 1687–1695.
135 D. Wakerley, S. Lamaison, F. Ozanam, N. Menguy, D. Mercier, P. Marcus, M. Fontecave and V. Mougel, *Nat. Mater.*, 2019, **18**, 1222–1227.
136 C. Kim, J. C. Bui, X. Luo, J. K. Cooper, A. Kusoglu, A. Z. Weber and A. T. Bell, *Nat. Energy*, 2021, **6**, 1026–1034.
137 M. Sadeghpour, R. Yusoff and M. K. Aroua, *Rev. Chem. Eng.*, 2017, **33**, 183–200.
138 K. Zhao and X. Quan, *ACS Catal.*, 2021, **11**, 2076–2097.
139 X. Duan, J. Xu, Z. Wei, J. Ma, S. Guo, S. Wang, H. Liu and S. Dou, *Adv. Mater.*, 2017, **29**, 1701784.
140 J. Wu, S. Ma, J. Sun, J. I. Gold, C. Tiwary, B. Kim, L. Zhu, N. Chopra, I. N. Odeh, R. Vajtai, A. Z. Yu, R. Luo, J. Lou, G. Ding, P. J. Kenis and P. M. Ajayan, *Nat. Commun.*, 2016, **7**, 13869–13875.
141 X. Zou, M. Liu, J. Wu, P. M. Ajayan, J. Li, B. Liu and B. I. Yakobson, *ACS Catal.*, 2017, **7**, 6245–6250.
142 Y. Liu, S. Chen, X. Quan and H. Yu, *J. Am. Chem. Soc.*, 2015, **137**, 11631–11636.
143 Y. Liu, Y. Zhang, K. Cheng, X. Quan, X. Fan, Y. Su, S. Chen, H. Zhao, Y. Zhang, H. Yu and M. R. Hoffmann, *Angew. Chem., Int. Ed.*, 2017, **56**, 15607–15611.

144 Y. Song, W. Chen, C. Zhao, S. Li, W. Wei and Y. Sun, *Angew. Chem., Int. Ed.*, 2017, **56**, 10840–10844.
145 Y. Song, S. Wang, W. Chen, S. Li, G. Feng, W. Wei and Y. Sun, *ChemSusChem*, 2020, **13**, 293–297.
146 D. Higgins, C. Hahn, C. Xiang, T. F. Jaramillo and A. Z. Weber, *ACS Energy Lett.*, 2018, **4**, 317–324.
147 L. C. Weng, A. T. Bell and A. Z. Weber, *Phys. Chem. Chem. Phys.*, 2018, **20**, 16973–16984.
148 T. N. Nguyen and C. T. Dinh, *Chem. Soc. Rev.*, 2020, **49**, 7488–7504.
149 W. Ma, S. Xie, T. Liu, Q. Fan, J. Ye, F. Sun, Z. Jiang, Q. Zhang, J. Cheng and Y. Wang, *Nat. Catal.*, 2020, **3**, 478–487.
150 R. Chen, H. Y. Su, D. Liu, R. Huang, X. Meng, X. Cui, Z. Q. Tian, D. H. Zhang and D. Deng, *Angew. Chem., Int. Ed.*, 2020, **59**, 154–160.
151 E. W. Lees, B. A. W. Mowbray, D. A. Salvatore, G. L. Simpson, D. J. Dvorak, S. Ren, J. Chau, K. L. Milton and C. P. Berlinguette, *J. Mater. Chem. A*, 2020, **8**, 19493–19501.
152 T. Möller, T. Ngo Thanh, X. Wang, W. Ju, Z. Jovanov and P. Strasser, *Energy Environ. Sci.*, 2021, **14**, 5995–6006.
153 D. Wakerley, S. Lamaison, J. Wicks, A. Clemens, J. Feaster, D. Corral, S. A. Jaffer, A. Sarkar, M. Fontecave, E. B. Duoss, S. Baker, E. H. Sargent, T. F. Jaramillo and C. Hahn, *Nat. Energy*, 2022, **7**, 130–143.
154 D. Salvatore and C. P. Berlinguette, *ACS Energy Lett.*, 2019, **5**, 215–220.
155 B. Endrődi, E. Kecsenovity, A. Samu, T. Halmágyi, S. Rojas-Carbonell, L. Wang, Y. Yan and C. Janáky, *Energy Environ. Sci.*, 2020, **13**, 4098–4105.
156 A. Gawel, T. Jaster, D. Siegmund, J. Holzmann, H. Lohmann, E. Klemm and U. P. Apfel, *iScience*, 2022, **25**, 104011.
157 R. K. Miao, Y. Xu, A. Ozden, A. Robb, C. P. O'Brien, C. M. Gabardo, G. Lee, J. P. Edwards, J. E. Huang, M. Fan, X. Wang, S. Liu, Y. Yan, E. H. Sargent and D. Sinton, *Joule*, 2021, **5**, 2742–2753.
158 M. E. Leonard, L. E. Clarke, A. Forner-Cuenca, S. M. Brown and F. R. Brushett, *ChemSusChem*, 2020, **13**, 400–411.
159 Y. Chen, A. Vise, W. E. Klein, F. C. Cetinbas, D. J. Myers, W. A. Smith, T. G. Deutsch and K. C. Neyerlin, *ACS Energy Lett.*, 2020, **5**, 1825–1833.
160 M. A. Blommaert, D. Aili, R. A. Tufa, Q. Li, W. A. Smith and D. A. Vermaas, *ACS Energy Lett.*, 2021, **6**, 2539–2548.
161 J. E. Huang, F. Li, A. Ozden, A. S. Rasouli, F. P. G. de Arquer, S. Liu, S. Zhang, M. Luo, X. Wang and Y. Lum, *Science*, 2021, **372**, 1074–1078.
162 O. Romiluyi, N. Danilovic, A. T. Bell and A. Z. Weber, *Electrochem. Sci. Adv.*, 2022, e2100186.
163 B. Endrodi, E. Kecsenovity, A. Samu, F. Darvas, R. V. Jones, V. Torok, A. Danyi and C. Janaky, *ACS Energy Lett.*, 2019, **4**, 1770–1777.
164 D. M. Weekes, D. A. Salvatore, A. Reyes, A. Huang and C. P. Berlinguette, *Acc. Chem. Res.*, 2018, **51**, 910–918.
165 C. M. Gabardo, A. Seifitokaldani, J. P. Edwards, C.-T. Dinh, T. Burdyny, M. G. Kibria, C. P. O'Brien, E. H. Sargent and D. Sinton, *Energy Environ. Sci.*, 2018, **11**, 2531–2539.
166 S. Ringe, E. L. Clark, J. Resasco, A. Walton, B. Seger, A. T. Bell and K. Chan, *Energy Environ. Sci.*, 2019, **12**, 3001–3014.
167 A. G. Fink, E. W. Lees, Z. Zhang, S. Ren, R. S. Delima and C. P. Berlinguette, *ChemElectroChem*, 2021, **8**, 2094–2100.
168 M. C. O. Monteiro, F. Dattila, B. Hagedoorn, R. García-Muelas, N. López and M. T. M. Koper, *Nat. Catal.*, 2021, **4**, 654–662.
169 B. Endrodi, A. Samu, E. Kecsenovity, T. Halmagyi, D. Sebok and C. Janáky, *Nat. Energy*, 2021, **6**, 439–448.
170 P. K. Giesbrecht and M. S. Freund, *Chem. Mater.*, 2020, **32**, 8060–8090.
171 C. Shen, R. Wycisk and P. N. Pintauro, *Energy Environ. Sci.*, 2017, **10**, 1435–1442.
172 Y. Chen, J. A. Wrubel, W. E. Klein, S. Kabir, W. A. Smith, K. Neyerlin and T. G. Deutsch, *ACS Appl. Polym. Mater.*, 2020, **2**, 4559–4569.
173 G. Li, M. A. Shehzad, Z. Ge, H. Wang, A. Yasmin, X. Yang, X. Ge, L. Wu and T. Xu, *Sep. Purif. Technol.*, 2021, **275**, 119167.
174 Z. Ge, M. A. Shehzad, L. Ge, Y. Zhu, H. Wang, G. Li, J. Zhang, X. Ge, L. Wu and T. Xu, *ACS Appl. Energy Mater.*, 2020, **3**, 5765–5773.
175 M. A. Shehzad, A. Yasmin, X. Ge, Z. Ge, K. Zhang, X. Liang, J. Zhang, G. Li, X. Xiao and B. Jiang, *Nat. Commun.*, 2021, **12**, 4652–4671.
176 K. Yang, M. Li, S. Subramanian, M. A. Blommaert, W. A. Smith and T. Burdyny, *ACS Energy Lett.*, 2021, **6**, 4291–4298.
177 Z. Yan, J. L. Hitt, Z. Zeng, M. A. Hickner and T. E. Mallouk, *Nat. Chem.*, 2021, **13**, 33–40.
178 D. T. Whipple, E. C. Finke and P. J. Kenis, *Electrochem. Solid-State Lett.*, 2010, **13**, B109.
179 R. S. Jayashree, S. K. Yoon, F. R. Brushett, P. O. Lopez-Montesinos, D. Natarajan, L. J. Markoski and P. J. A. Kenis, *J. Power Sources*, 2010, **195**, 3569–3578.
180 X. Lu, D. Y. C. Leung, H. Wang, M. M. Maroto-Valer and J. Xuan, *Renewable Energy*, 2016, **95**, 277–285.
181 X. Lu, Y. Wang, D. Y. C. Leung, J. Xuan and H. Wang, *Appl. Energy*, 2018, **217**, 241–248.
182 X. Lu, D. Y. C. Leung, H. Wang and J. Xuan, *Appl. Energy*, 2017, **194**, 549–559.
183 H. Wang, D. Y. C. Leung and J. Xuan, *Appl. Energy*, 2013, **102**, 1057–1062.
184 K. Wu, E. Birgersson, B. Kim, P. J. A. Kenis and I. A. Karimi, *J. Electrochem. Soc.*, 2015, **162**, F23–F32.
185 J. P. Edwards, Y. Xu, C. M. Gabardo, C.-T. Dinh, J. Li, Z. Qi, A. Ozden, E. H. Sargent and D. Sinton, *Appl. Energy*, 2020, **261**, 114305.
186 H. Yang, J. J. Kaczur, S. D. Sajjad and R. I. Masel, *J. CO2 Util.*, 2017, **20**, 208–217.
187 H. Yang, J. J. Kaczur, S. D. Sajjad and R. I. Masel, *J. CO2 Util.*, 2020, **42**, 101349–101357.

188 L. Fan, C. Xia, P. Zhu, Y. Lu and H. Wang, *Nat. Commun.*, 2020, **11**, 3633–3640.
189 C. Xia, P. Zhu, Q. Jiang, Y. Pan, W. Liang, E. Stavitski, H. N. Alshareef and H. Wang, *Nat. Energy*, 2019, **4**, 776–785.
190 R. Buonsanti, *Nat. Energy*, 2019, **4**, 728–729.
191 P. Zhu and H. Wang, *Nat. Catal.*, 2021, **4**, 943–951.
192 X. Zhang, Y. Song, G. Wang and X. Bao, *J. Energy Chem.*, 2017, **26**, 839–853.
193 Y. Tian, N. Abhishek, C. Yang, R. Yang, S. Choi, B. Chi, J. Pu, Y. Ling, J. T. S. Irvine and G. Kim, *Matter*, 2022, **5**, 482–514.
194 A. Ozden, Y. Wang, F. Li, M. Luo, J. Sisler, A. Thevenon, A. Rosas-Hernández, T. Burdyny, Y. Lum, H. Yadegari, T. Agapie, J. C. Peters, E. H. Sargent and D. Sinton, *Joule*, 2021, **5**, 706–719.